Check for updates

International Journal for Numerical Methods in Engineering

WILEY

RESEARCH ARTICLE OPEN ACCESS

Space-Time Boundary Elements on Graded Meshes for 3D Elastodynamics

Alessandra Aimi[1] | Luca Desiderio[2] | Heiko Gimperlein[3] | Chiara Guardasoni[1]

[1]Department of Mathematical, Physical and Computer Sciences, University of Parma, Parma, Italy | [2]Department of Mathematics and Computer Sciences, Physical Sciences and Earth Sciences, University of Messina, Messina, Italy | [3]Engineering Mathematics, University of Innsbruck, Innsbruck, Austria

Correspondence: Heiko Gimperlein (heiko.gimperlein@uibk.ac.at)

Received: 18 March 2025 | **Revised:** 27 August 2025 | **Accepted:** 9 October 2025

Funding: This work was supported by the Gruppo Nazionale per il Calcolo Scientifico (Grant No. CUP E53C24001950001) and the European Commission (Grant No. CUP B83C22002830001).

Keywords: 3D elastodynamics | geometric singularities | graded meshes | space-time boundary elements

ABSTRACT

The solution to the elastodynamic equations in the exterior of a polygonal or polyhedral domain or a screen exhibits singularities at corners and edges. This paper presents a space-time boundary element method in 3D on algebraically graded meshes to resolve these singularities, based on recently obtained error estimates for the weakly singular integral equation. Numerical examples show the efficiency of the proposed approach. They confirm the theoretically predicted, quasi-optimal convergence rates and study the singular behavior of the solution for typical 3D geometries with edges, corners or cone points.

1 | Introduction

The displacement and stress of an elastic body exhibit singular behavior from edges, corners or cone points. Their asymptotic behavior near such geometric singularities is well-understood for static problems [1–3]. Numerically, singular expansions of the displacement and stresses are the basis of efficient approximations by h, p and hp finite [4] or boundary element methods [5], which recover the optimal convergence rates known for smooth solutions.

Corresponding methods for elastodynamic problems are only starting to be explored. Foundational works by Plamenevskiĭ and collaborators, [6, 7] demonstrate that the transient displacement and stresses exhibit singular behavior of the same kind as in static problems. More precisely, their results imply that at any given time the transient singular expansions near an edge or a cone point involve the same singular functions known from the static case, with coefficients varying smoothly in time. Müller and Schwab [8] later used these analytical results to obtain optimal convergence rates

A. Aimi, L. Desiderio, C. Guardasoni are members of INdAM-GNCS Research Group, Italy. L. Desiderio is member of Accademia Peloritana dei Pericolanti, Messina, Italy.

This is an open access article under the terms of the Creative Commons Attribution-NonCommercial-NoDerivs License, which permits use and distribution in any medium, provided the original work is properly cited, the use is non-commercial and no modifications or adaptations are made.
© 2025 The Author(s). *International Journal for Numerical Methods in Engineering* published by John Wiley & Sons Ltd.

for a finite element method on graded meshes in 2D polygonal domains. Recent work by Aimi, Di Credico, Gimperlein and Stephan [9] extends the theoretical analysis to h and hp boundary element methods for elastodynamics, confirmed by numerical experiments in 2D model cases. Beyond elastodynamics, the asymptotic behavior and numerical approximation of solutions with geometric singularities using graded meshes, has been of much recent interest in the context of time dependent problems [8, 10–13], with numerical studies mostly restricted to 2D. Most closely related to the current work, [14] considers the 3D scalar wave equation outside a flat screen.

In this article we study h-versions of the boundary element method for elastodynamics in 3D polyhedral domains or, as the most challenging case, in the complement of a polygonal screen. The singular expansion of the boundary traction leads to quasi-optimal convergence rates for boundary element approximations on *time independent* algebraically graded meshes. Detailed numerical experiments present the first rigorous computational results for 3D elastodynamics. They confirm the predicted convergence rates and the precise singular behavior of the solutions. Empirically, they demonstrate the computational savings and achievable accuracies in transient problems. Moreover, algorithmic issues are clarified, including for example, relevant aspects of the required numerical quadrature and time step size.

To be specific, we consider elastodynamic wave propagation in a polyhedral domain or outside a polygonal screen, with prescribed displacement on the boundary Γ. To solve this problem numerically, we formulate it as an equivalent time-dependent integral equation for the single layer operator on the boundary. Its solution is numerically approximated using a space-time Galerkin boundary element method based on tensor product elements on a quasi-uniform or graded mesh for Γ in space and a uniform mesh in time.

As obtained in [9], the approximation rate is governed by the above-mentioned geometric singularities of the traction on the boundary. We review the behavior of traction and displacement for typical singular 3D geometries and, in a Theorem in Section 5.2, deduce an a priori error estimate for the error of the h-method on algebraically graded meshes. Essentially, the convergence rate on β-graded meshes (defined in Section 5.1) is improved by a factor β with respect to the rate on quasi-uniform meshes, until the quasi-optimal rate $\frac{3}{2}$ is achieved for large β. Note that, unlike in two space dimensions, quasi-optimal convergence rates cannot be obtained on shape-regular meshes: the thin, anisotropic elements of a graded mesh are required for the quasi-optimal approximation of edge singularities.

Detailed numerical experiments are presented in typical 3D geometries with edges, corners or cone points. They study the convergence rates on algebraically graded and quasi-uniform meshes for these singular geometries, as well as the leading singular behavior of the solution. The numerical results underline the theoretical predictions. They further demonstrate the possible use of large time steps, in spite of the resulting locally large CFL ratios. Also, relevant aspects of the numerical quadrature are discussed.

Our work contributes to the active developments in boundary element methods for acoustic and elastodynamic wave equations based on both space-time Galerkin and convolution quadrature methods, see [15–18] for an overview. Our approach is based on formulations related to the energy of the system [19], which assures unconditional stability. The application of boundary element methods to problems in elastodynamics has a long history in engineering [20], and the mathematical analysis was started in [21, 22] for scattering and for crack problems. Recent works on the numerical analysis and computational aspects of elastodynamic problems include [9, 23–27].

For time independent elastic problems in polygonal or polyhedral domains, the study of singular expansions near non-smooth boundary points has a long history, partly motivated by the difficulty to compute quantities of interest like stress intensity factors. Beyond the general references mentioned at the beginning of this Introduction, we refer to [28–33] for examples and applications motivating the current work. Based on such expansions, von Petersdorff [34] first derived quasi-optimal convergence rates for boundary elements on algebraically graded meshes for the Laplace equation, Thereby, he generalized fundamental best-approximation results for finite element spaces in the H^1-norm, in particular in [35], to the fractional Sobolev norms relevant for boundary element approximations. See also [36] for a complementary perspective motivated by geometric analysis and [37, 38] for an overview.

The article is organized as follows: after presenting the model problem in the Section 2, Section 3 reviews the singular expansion of displacement and stress near non-smooth boundary points, like edges, corners and cone points. The weak formulation of the boundary integral equation is discussed in Section 4. Section 5 then introduces the boundary element discretization based on piece-wise polynomial approximations of the solution for uniform time steps and algebraically graded meshes in space. It presents an a priori error estimate, showing a quasi-optimal convergence rate, and discusses

10970207, 2025, 20, Downloaded from https://onlinelibrary.wiley.com/doi/10.1002/nme.70163 by University Degli Studi Di Messina, Wiley Online Library on [16/11/2026]. See the Terms and Conditions (https://onlinelibrary.wiley.com/terms-and-conditions) on Wiley Online Library for rules of use; OA articles are governed by the applicable Creative Commons License

the algorithmic realization of the proposed approach. Detailed numerical results are the content of Section 6. Section 7 outlines our conclusions. The relevant definitions of function spaces and norms that are used in the analysis are recalled in Appendix A.

2 | Model Problem

In the Euclidean space $\mathbb{R}^3$ equipped with a fixed orthonormal Cartesian coordinate system $\mathbf{x} = \left(x_1, x_2, x_3\right)^\top$ with origin at $\mathbf{O} = (0,0,0)^\top$, we consider a screen or a closed surface Γ and its connected exterior, denoted by Ω. Further, let $J := [0,T]$ be a time interval for a given final time instant $T > 0$. Under the assumptions of small displacement theory and in absence of external sources, elastodynamic wave propagation is described by the following boundary value problem for the Navier-Cauchy equation of motion:

$$\begin{cases} \varrho\ddot{\mathbf{u}}(\mathbf{x};t) - \boldsymbol{\nabla}\cdot\boldsymbol{\sigma}[\mathbf{u}](\mathbf{x};t) = \mathbf{0} & (\mathbf{x};t)\in\Omega\times J \quad (2.1a)\\ \mathbf{u}(\mathbf{x};t) = \overline{\mathbf{u}}(\mathbf{x};t) & (\mathbf{x};t)\in\Gamma\times J \quad (2.1b)\\ \mathbf{u}(\mathbf{x};0) = \mathbf{0} & \mathbf{x}\in\Omega \quad (2.1c)\\ \dot{\mathbf{u}}(\mathbf{x};0) = \mathbf{0} & \mathbf{x}\in\Omega, \quad (2.1d) \end{cases}$$

Where $\mathbf{u}(\mathbf{x};t) = \left(u_1,u_2,u_3\right)^\top(\mathbf{x};t)$ and $\boldsymbol{\sigma}[\mathbf{u}](\mathbf{x};t)$ represent, respectively, the unknown displacement field and the stress tensor at point $\mathbf{x}$ and time t. In addition, ϱ is the mass density of the medium occupying Ω. In problem (2.1), homogeneous initial conditions are assumed at the first time of interest $t = 0$ and a Dirichlet type boundary condition $\overline{\mathbf{u}}(\mathbf{x};t) = \left(\bar{u}_1,\bar{u}_2,\bar{u}_3\right)^\top(\mathbf{x};t)$ is prescribed on Γ. Furthermore, the superposed dot indicates time differentiation, while $\boldsymbol{\nabla}$ denotes the nabla operator. According to linear elasticity theory, the stress-strain relation allows us to express the tensor $\boldsymbol{\sigma}[\mathbf{u}]$ as follows:

$$\boldsymbol{\sigma}[\mathbf{u}](\mathbf{x};t) := \lambda[\boldsymbol{\nabla}\cdot\mathbf{u}(\mathbf{x};t)]\mathbf{I} + \mu\left[\boldsymbol{\nabla}\mathbf{u}(\mathbf{x};t) + \boldsymbol{\nabla}\mathbf{u}^\top(\mathbf{x};t)\right], \tag{2.2}$$

$\mathbf{I}$ being the 3-by-3 identity tensor, while μ and λ being the shear modulus and the Lamé parameter, respectively. Since we can separate equation (2.1a) into solutions for the pressure wave (P-wave in short) and the shear wave (S-wave in short) by taking the divergence and curl respectively, the elastic parameters μ and λ are related to the primary and secondary wave speeds $c_{\mathrm{P}}^2 := (\lambda+2\mu)\varrho^{-1}$ and $c_{\mathrm{S}}^2 := \mu\varrho^{-1}$.

A crucial property of the Navier-Cauchy equation is the energy balance. For all $t\in J$ the time-dependent energy functional is defined as the sum of the kinetic energy and the total strain energy [39], that is:

$$E(t) := \frac{1}{2}\left\{\int_\Omega \dot{\mathbf{u}}^2(\mathbf{x};t)\mathrm{d}\mathbf{x} + c_{\mathrm{S}}^2\int_\Omega \boldsymbol{\nabla}\mathbf{u}(\mathbf{x};t) : \boldsymbol{\nabla}\mathbf{u}(\mathbf{x};t)\mathrm{d}\mathbf{x} + (c_{\mathrm{P}}^2 - c_{\mathrm{S}}^2)\int_\Omega [\boldsymbol{\nabla}\cdot\mathbf{u}(\mathbf{x};t)]^2\mathrm{d}\mathbf{x}\right\}, \tag{2.3}$$

where the symbol : stands for the double inner tensor product. Testing (2.1a) against $\dot{\mathbf{u}}(\mathbf{x};t)$, integrating over Ω and using Green's formula implies that

$$\frac{d}{dt}E(t) = \int_\Gamma \mathbf{p}(\mathbf{u})^\top(\mathbf{x};t)\dot{\mathbf{u}}(\mathbf{x};t)\mathrm{d}\Gamma_{\mathbf{x}} \tag{2.4}$$

where $\mathbf{p}(\mathbf{u})(\mathbf{x};t)$ stands for the traction vector $\boldsymbol{\sigma}[\mathbf{u}](\mathbf{x};t)\cdot\mathbf{n}_{\mathbf{x}}$ (in case of a screen, if Γ^- and Γ^+ denote respectively the lower and the upper face of Γ, then $\mathbf{n}_{\mathbf{x}}$ is oriented from Γ^- to Γ^+).

Integrating the relationship (2.4) over J, the homogeneous initial conditions allow us to derive the following energy balance equation:

$$E(T) = \int_0^T\int_\Gamma \mathbf{p}(\mathbf{u})^\top(\mathbf{x};t)\dot{\mathbf{u}}(\mathbf{x};t)\mathrm{d}\Gamma_{\mathbf{x}}\mathrm{d}t. \tag{2.5}$$

To solve (2.1) numerically, we formulate it as an equivalent time dependent integral equation on $\Gamma\times J$, as briefly recalled in the following Section 4, that is, we study

$$\mathbf{V}[\mathbf{w}](\mathbf{x};t) = \left(\mathbf{K} + \tfrac{1}{2}\mathbf{I}\right)[\overline{\mathbf{u}}](\mathbf{x};t), \qquad (\mathbf{x},t)\in\Gamma\times J\ , \tag{2.6}$$

10970207, 2025, 20, Downloaded from https://onlinelibrary.wiley.com/doi/10.1002/nme.70163 by University Degli Studi Di Messina, Wiley Online Library on [16/11/2026]. See the Terms and Conditions (https://onlinelibrary.wiley.com/terms-and-conditions) on Wiley Online Library for rules of use; OA articles are governed by the applicable Creative Commons License

where $\mathbf{w} := \mathbf{p}(\mathbf{u})_{|\Gamma\times J}$, involving the weakly singular integral operator $\mathbf{V}$ and, on the right-hand side the double layer integral operator $\mathbf{K}$, defined from a fundamental solution $\mathbf{G}$ to (2.1a) and its traction $\mathbf{p}_{\mathbf{y}}(\mathbf{G})$, respectively, as

$$\mathbf{V}[\mathbf{\Phi}](\mathbf{x};t) = \int_0^t \int_\Gamma \mathbf{G}(\mathbf{x},\mathbf{y};t,\tau)\mathbf{\Phi}(\mathbf{y};\tau)d\Gamma_{\mathbf{y}}d\tau\ ,$$
$$\mathbf{K}[\mathbf{\Psi}](\mathbf{x};t) = \int_0^t \int_\Gamma \mathbf{p}_{\mathbf{y}}(\mathbf{G})(\mathbf{x},\mathbf{y};t,\tau)^T\mathbf{\Psi}(\mathbf{y},\tau)d\Gamma_{\mathbf{y}}d\tau\ .$$

Kernel tensor $\mathbf{G}$ represents the response of the elastic medium to a unidirectional unit δ-Dirac impulse in space and time. In particular, its entries:

$$G_{ij}(\mathbf{x},\mathbf{y};t,\tau) := \frac{1}{4\pi\rho c_{\mathrm{P}}^2}\frac{r_i r_j}{r^3}\delta\left(t-\tau-\frac{r}{c_{\mathrm{P}}}\right) + \frac{1}{4\pi\rho c_{\mathrm{S}}^2}\left(\frac{\delta_{ij}}{r}-\frac{r_i r_j}{r^3}\right)\delta\left(t-\tau-\frac{r}{c_{\mathrm{S}}}\right)+$$
$$-\frac{1}{4\pi\rho}\left(\frac{\delta_{ij}}{r^3}-\frac{r_i r_j}{r^5}\right)(t-\tau)\left[H\left(t-\tau-\frac{r}{c_{\mathrm{P}}}\right)-H\left(t-\tau-\frac{r}{c_{\mathrm{S}}}\right)\right], \tag{2.7}$$

provide the i-th component of the displacement at the observation point $\mathbf{x}$ and observation time t, due to a force in the j-th direction at the source point $\mathbf{y}$ and emission time τ. Moreover, they depend only on the difference $\mathbf{r} := \mathbf{x}-\mathbf{y}$ and $t-\tau$, but not on the source point $\mathbf{y}$ and the emission time τ themselves. Note that in (2.7) $H(\cdot)$ is the Heaviside function, while $\delta(\cdot)$ is the Dirac impulse.

3 | Singular Expansion Near Non-Smooth Boundary Points

For the time independent Lamé equations of elastostatics in a singular domain, detailed asymptotic expansions of the solution at non-smooth boundary points have been studied extensively, partly motivated by applications to computing quantities of interest like stress intensity factors, see for example, [2, 31–33, 40]. We describe key results for the elastodynamic equations in geometries with edges, cone points or corners, as relevant to this article. There the solution admits a singular expansion into a leading part of explicit singular functions plus smoother remainder terms.

3.1 | 2D Sector/Polygon

3.1.1 | Elastostatic Equation

We first review the time independent Lamé equations in the simple case of a polygon or sector $\Omega \subset \mathbb{R}^2$. There the singular functions at a vertex V_j are explicitly given in polar coordinates (r,ϕ) centered at V_j, depending on the opening angle ω_j at the vertex and the elastic parameters. The result is the basis to describe edge singularities of domains in $\mathbb{R}^3$ and for the corresponding elastodynamic problems.

Proposition 3.1. *Near a vertex V_j, with interior opening angle ω_j, the solution $\mathbf{u} \in H^1(\Omega)^2$ of the time independent Lamé equations with sufficiently regular Dirichlet boundary data admits the decomposition*

$$\mathbf{u}(r,\phi) = \mathbf{u}_{0,j}(r,\phi) + \sum_k a_{jk}^* \mathbf{S}_{jk}^*(r,\phi)\chi_j(r) \tag{3.1}$$

with a regular part $\mathbf{u}_0 \in H^{1+s}(\Omega)^2$, $s>0$ depending on the boundary data, $a_{jk}^* \in \mathbb{C}$, the singular functions

$$\mathbf{S}_{jk}^*(r,\phi) = \begin{cases} r^{\nu_{jk}^*}\ \boldsymbol{\varphi}_{jk}^*(\phi), & \text{for } \nu_{jk}^* \notin \mathbb{N}, \\ r^{\nu_{jk}^*}\ \ln\ r\ \boldsymbol{\varphi}_{jk}^*(\phi) + r^{\nu_{jk}^*}\ \tilde{\boldsymbol{\varphi}}_{jk}^*(\phi), & \text{for } \nu_{jk}^* \in \mathbb{N} \end{cases} \tag{3.2}$$

with $\boldsymbol{\varphi}_{jk}^*, \tilde{\boldsymbol{\varphi}}_{jk}^*$ defined below, and χ_j smooth cut-off functions localized at V_j. The singular exponents $\nu_{jk}^* \in \mathbb{C}$ with $\mathrm{Re}\ \nu_{jk}^* > 0$ are solutions of the equations

$$\sin \nu_{jk}^* \omega_j = \pm\frac{\nu_{jk}^*}{k^*}\sin\omega_j, \tag{3.3}$$

10970207, 2025, 20, Downloaded from https://onlinelibrary.wiley.com/doi/10.1002/nme.70163 by University Degli Studi Di Messina, Wiley Online Library on [16/11/2026]. See the Terms and Conditions (https://onlinelibrary.wiley.com/terms-and-conditions) on Wiley Online Library for rules of use; OA articles are governed by the applicable Creative Commons License

where $k^* = 3 - 4\nu$ *and* $\nu := \frac{\lambda}{2\lambda+\mu}$ *is the Poisson ratio. The functions* $\boldsymbol{\varphi}^*_{jk}$ *with the components* $(\varphi^*_{jk})_r$ *in r-direction and* $(\varphi^*_{jk})_\phi$ *in* ϕ*-direction are of the form*

$$(\varphi^*_{jk})_r = A\cos(1+\nu^*_{jk})\phi + B\sin(1+\nu^*_{jk})\phi + C\cos(1-\nu^*_{jk})\phi + D\sin(1-\nu^*_{jk})\phi \tag{3.4}$$

$$(\varphi^*_{jk})_\phi = -A\sin(1+\nu^*_{jk})\phi + B\cos(1+\nu^*_{jk})\phi - \gamma_{jk}C\sin(1-\nu^*_{jk})\phi + \gamma_{jk}D\cos(1-\nu^*_{jk})\phi \tag{3.5}$$

with constants $A, B, C, D \in \mathbb{C}$ *depending on the material parameters and* $\gamma_{jk} = \frac{3+\nu^*_{jk}-4\nu}{3-\nu^*_{jk}-4\nu}$. *The functions* $\tilde{\boldsymbol{\varphi}}^*_{jk}$ *are a linear combination of* $\cos((1\pm\nu^*_{jk})\phi)$, $\phi\cos((1\pm\nu^*_{jk})\phi)$, $\sin((1\pm\nu^*_{jk})\phi)$ *and* $\phi\sin((1\pm\nu^*_{jk})\phi)$.

3.1.2 | Elastodynamic Equation

The singular behavior of the solution to the elastodynamic equations is then studied using a Fourier transform in time [7–9]. In particular, Corollary 3.6 in [9] finds that in a neighborhood of V_j the solution to the elastodynamic equations admits the expansion

$$\mathbf{u}(r,\phi,\ t) = \mathbf{u}_0(r,\phi,t) + \sum_k (Xc^*_{jk})(r,\phi,\ t)\mathbf{S}^*_{jk}(r,\phi), \tag{3.6}$$

for suitable c^*_{jk} involving the same singular functions $\mathbf{S}^*_{jk}$ and singular exponents ν^*_{jk} as the time independent problem. The smoothing operator X is here given by

$$Xc(r,\phi,\ t) = \mathcal{F}^{-1}_{\tau\to t}(\chi(|\tau|r\cos\phi, |\tau|r\sin\phi)\ \hat{c}(\tau)),$$

with a suitable cut-off function χ.

3.1.3 | Laplace and Scalar Wave Equations

We also require a corresponding description of the singularities for the scalar wave equation

$$\varrho\partial_t^2 u - \Delta u = 0\ ,$$

with Dirichlet boundary conditions imposed near a vertex V_j of Ω. For the time independent problem

$$-\Delta u = 0\ ,$$

near V_j the solution u admits the decomposition

$$u(r,\phi) = u_0(r,\phi) + \sum_k a_{jk}S_{jk}(r,\phi)\chi_j(r) \tag{3.7}$$

analogous to Proposition 3.1, with the singular functions now given by

$$S_{jk}(r,\phi) = \begin{cases} r^{\nu_{jk}}\varphi_{jk}(\phi), & \text{for } \nu_{jk}\notin\mathbb{N}, \\ r^{\nu_{jk}}\ln r\ \varphi_{jk}(\phi) + r^{\nu_{jk}}\tilde{\varphi}_{jk}(\phi), & \text{for } \nu_{jk}\in\mathbb{N}. \end{cases} \tag{3.8}$$

The singular exponents are explicitly computable as $\nu_{jk} = \frac{k\pi}{\omega_j}$, $\varphi_{jk}(\phi) = \sin(\nu_{jk}\phi)$ and $\tilde{\varphi}_{jk}(\phi) = \cos(\nu_{jk}\phi)$, $k\in\mathbb{N}$.

The singular expansion (3.7) for the time independent problem translates into an expansion for the time dependent problem, analogous to (3.6), but with the singular functions S_{jk} replacing $\mathbf{S}^*_{jk}$ and suitable coefficients c_{jk} replacing c^*_{jk}.

10970207, 2025, 20, Downloaded from https://onlinelibrary.wiley.com/doi/10.1002/nme.70163 by University Degli Studi Di Messina, Wiley Online Library on [16/11/2026]. See the Terms and Conditions (https://onlinelibrary.wiley.com/terms-and-conditions) on Wiley Online Library for rules of use; OA articles are governed by the applicable Creative Commons License

3.2 | 3D Wedge

The behavior of solutions in a wedge of opening angle ω, denoted by $\Omega = \mathbb{K} \times \mathbb{R}$ with $\mathbb{K} = \{(r, \phi) : r > 0,\ \phi \in (0, \omega)\}$, generalizes the discussion in Section 3.1 from dimension $n = 2$ to $n = 3$. As an example, the wedge $\mathbb{K} \times \mathbb{R}$ is a model for the curved edge between the base and the lateral surface of the cone illustrated in Figure 1. We omit the index j in the discussion for polygons, as long as we consider the model geometry with only one non-smooth subset $\{\mathbf{0}\} \times \mathbb{R}$ of $\partial\Omega$. For the time dependent problem the singular expansion of the solution near the edge $\{\mathbf{0}\} \times \mathbb{R}$ is given by, in cylindrical coordinates and denoting by x_3 the coordinate along the edge of the wedge:

$$\mathbf{u}(r, \phi, x_3, t) = \mathbf{u}_0(r, \phi, x_3, t) + \sum_{k,\ell} (Xc_{k\ell})(r, \phi, x_3, t)\mathbf{S}_{k\ell}(r, \phi) + \sum_{k,\ell} (Xc^*_{k\ell})(r, \phi, x_3, t)\mathbf{S}^*_{k\ell}(r, \phi). \tag{3.9}$$

Here, the singular functions $\mathbf{S}_{k\ell}$ and $\mathbf{S}^*_{k\ell}$ are constructed from those in Section 3.1 ((3.8), respectively (3.2)). The smoothing operator X for the edge is given by

$$Xc(r, \phi, x_3, t) = \mathcal{F}^{-1}_{(\xi,\tau)\to(x_3,t)}\Big(\chi(\sqrt{|\xi|^2 + |\tau|^2}(r\cos\phi, r\sin\phi))\hat{c}(\xi, \tau)\Big)$$

for $\hat{c} = \hat{c}_{k\ell}, \hat{c}^*_{k\ell}$. We refer to Section 3.2 in [9] and to [7] for a detailed analysis.

By considering the coordinate x_3 along the edge as a parameter, the expansion recovers those for polygonal domains in $\mathbb{R}^2$ in Section 3.1.

Applications to boundary integral equations require the Neumann trace of the solution $\mathbf{u}$ of the inhomogeneous Dirichlet problem and the given initial conditions. As in (3.9), we obtain the leading singular behavior

$$\mathbf{w}(r, \phi, x_3, t) = \mathbf{b}(\phi, x_3, t)r^{\nu^*-1} + \mathbf{w}_0(r, \phi, x_3, t). \tag{3.10}$$

Here, ν^* denotes the leading singular exponent, $\mathbf{b}$ is smooth for smooth data and $\mathbf{w}_0$ is a less singular remainder.

3.3 | 3D Cone

We now consider the elastodynamic equations in the exterior of an infinitely extended cone $\mathbb{K}$ with vertex at $r = 0$ and opening angle Θ. The model geometry of a finitely extended cone of opening angle Θ is illustrated at the top of Figure 1. The singular behavior of solutions to the elastostatic Lamé equations has been studied, in particular, in [30, 31], in dependence on Θ and the elastic parameters.

Using spherical coordinates (r, ϕ, θ), local orthonormal basis vectors are given by

$$\begin{aligned}
\mathbf{e}_r &= (\sin(\theta)\cos(\phi), \sin(\theta)\sin(\phi), \cos(\theta))^\top,\\
\mathbf{e}_\theta &= (\cos(\theta)\cos(\phi), \cos(\theta)\sin(\phi), -\sin(\theta))^\top,\\
\mathbf{e}_\phi &= (-\sin(\phi), \cos(\phi), 0)^\top.
\end{aligned}$$

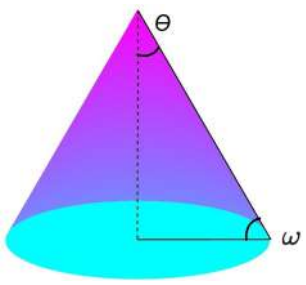

FIGURE 1 | Model geometry of a 3d cone with opening angle Θ. This includes also a curved wedge, between the lateral surface and the basis, of opening angle ω.

10970207, 2025, 20, Downloaded from https://onlinelibrary.wiley.com/doi/10.1002/nme.70163 by University Degli Studi Di Messina, Wiley Online Library on [16/11/2026]. See the Terms and Conditions (https://onlinelibrary.wiley.com/terms-and-conditions) on Wiley Online Library for rules of use; OA articles are governed by the applicable Creative Commons License

We write the components of a vector $\mathbf{u}$ in this basis as $\mathbf{u} = u_r\mathbf{e}_r + u_\theta\mathbf{e}_\theta + u_\phi\mathbf{e}_\phi$. For the time independent problem Beagles and Sändig [31] use Papkovich-Neuber potentials to construct the general form of rotationally symmetric solutions from the ansatz

$$\mathbf{u} = 4(1-\nu)\mathbf{B} - \nabla(\mathbf{x}\cdot\mathbf{B} + B_4) \tag{3.11}$$

with Poisson's ratio ν and where the components of $\mathbf{B} = (B_1, B_2, B_3)^\top$ and B_4 are harmonic functions. In spherical coordinates the ansatz (3.11) is written as

$$\begin{aligned}\mathbf{u} = (u_r, u_\theta, u_\phi)^\top &= (3-4\nu)(\mathbf{B}\cdot\mathbf{e}_r, \mathbf{B}\cdot\mathbf{e}_\theta, \mathbf{B}\cdot\mathbf{e}_\phi)^\top \\ &\quad - (r\mathbf{e}_r\cdot\partial_r\mathbf{B} + \partial_r B_4, \mathbf{e}_r\cdot\partial_\theta\mathbf{B} + \frac{1}{r}\partial_\theta B_4, \frac{1}{\sin(\theta)}\mathbf{e}_r\cdot\partial_\phi\mathbf{B} + \frac{1}{r\sin(\theta)}\partial_\phi B_4)^\top.\end{aligned} \tag{3.12}$$

To find the rotationally symmetric solutions (which also describe the generic leading behavior), we set $B_1 = B_2 = 0$,

$$B_3 = c_1 r^\alpha P_\alpha(\cos(\theta)),\quad B_4 = c_2 r^{\alpha+1} P_{\alpha+1}(\cos(\theta)),$$

where $P_\alpha(\cos(\theta))$ are Legendre functions of the first kind and the singular exponent $\alpha > 0$ together with the coefficients c_1, c_2 are obtained below. Substitution into (3.12) gives the singular functions for the cone

$$\mathbf{u}(r,\theta) = c_1 r^\alpha \begin{pmatrix} A_{11}(\alpha,\theta) \\ A_{21}(\alpha,\theta)\end{pmatrix} + c_2 r^\alpha \begin{pmatrix} B_{11}(\alpha,\theta) \\ B_{21}(\alpha,\theta)\end{pmatrix} \tag{3.13}$$

with

$$(A_{11}(\alpha,\theta), A_{21}(\alpha,\theta)) = \big((3-4\nu-\alpha)P_\alpha(\cos(\theta)), P'_\alpha(\cos(\theta))\cos(\theta)\sin(\theta) - (3-4\nu)P_\alpha(\cos(\theta))\sin(\theta)\big),$$

as well as $(B_{11}(\alpha,\theta), B_{21}(\alpha,\theta)) = \big(-(\alpha+1)P_{\alpha+1}(\cos(\theta)), \sin(\theta)P'_{\alpha+1}(\cos(\theta))\big)$. The singular exponents α are computed as the roots of the equation

$$\det\begin{pmatrix} A_{11}(\alpha,\Theta) & B_{11}(\alpha,\Theta) \\ A_{21}(\alpha,\Theta) & B_{21}(\alpha,\Theta)\end{pmatrix} = 0\ .$$

Substituting for $A_{11}, A_{21}, B_{11}, B_{21}$, this equation for α takes the following form:

$$\begin{aligned}0 = \frac{-(\alpha+1)}{\sin(\Theta)}\big(&P_\alpha^2(\cos(\Theta))\cos(\Theta)(\alpha+4\nu-3) \\ &+P_\alpha(\cos(\Theta))P_{\alpha+1}(\cos(\Theta))(3-4\nu-\cos^2(\Theta)(2\alpha+1)) + P_{\alpha+1}^2(\cos(\Theta))\cos(\Theta)(\alpha+1)\big)\ .\end{aligned} \tag{3.14}$$

Imposing homogeneous Dirichlet conditions on $\mathbf{u}$ in (3.13) determines the coefficients c_1, c_2 and hence the corresponding eigenfunction. We refer to [31] for numerical results for the zeros α and their dependence on the opening angle Θ and Poisson's ratio ν.

For the time independent problem, the singular expansion of the solution near the cone tip is based on the singular functions from (3.13) and the exponents α which are the roots in (3.14), and it can be expressed as

$$\mathbf{u}(r,\phi,\theta) = \sum_{k,\ell}\tilde{a}_\ell^k(\phi)\mathbf{u}_\ell^k(r,\theta) + \mathbf{u}_0(r,\phi,\theta). \tag{3.15}$$

The singular expansion translates into a singular expansion for the time dependent problem, see Section 3.3 in [9]:

$$\mathbf{u}(r,\phi,\theta,t) = \sum_{k,\ell}\tilde{c}_\ell^k(r,\phi,\theta,t)\mathbf{u}_\ell^k(r,\theta) + \mathbf{u}_0(r,\phi,\theta,t). \tag{3.16}$$

For applications to boundary integral equations we again require the Neumann trace at $\theta = \Theta$ of the solution $\mathbf{u}$ of the inhomogeneous Dirichlet problem with given initial conditions. For the cone we obtain the leading singular behavior

$$\mathbf{w}(r,\phi,t) = \chi(r)r^{\alpha-1}\mathbf{b}(\phi,t) + \mathbf{w}_0(r,\phi,t), \tag{3.17}$$

for the leading root α of (3.14) and a suitable cut-off function χ localized in a neighborhood of the cone tip, $r = 0$. Here, $\mathbf{b}$ is smooth for smooth data and $\mathbf{w}_0$ a less singular remainder.

10970207, 2025, 20, Downloaded from https://onlinelibrary.wiley.com/doi/10.1002/nme.70163 by University Degli Studi Di Messina, Wiley Online Library on [16/11/2026]. See the Terms and Conditions (https://onlinelibrary.wiley.com/terms-and-conditions) on Wiley Online Library for rules of use; OA articles are governed by the applicable Creative Commons License

For both the wedge and the cone, we may assume, after possibly expanding $\mathbf{w}_0$ further in (3.10), respectively (3.17), that the regular part $\mathbf{w}_0$ is sufficiently smooth in space. Corresponding expansions then also hold for the solutions $\mathbf{w}$ to the integral equation, see also (4.2).

3.4 | Polygonal Screens and Polyhedral Domains in 3D

Beyond the geometries considered in Sections 3.1 to 3.3, singularities at corner points are of significant interest. The simplest case is given by a flat polygonal screen $\Gamma \subset \mathbb{R}^3$, where singularities arise from the edges and corner points. For time independent problems in this geometry, asymptotic expansions and their implications for the numerical approximation are discussed, for example, in [1, 34]. For the time dependent scalar wave equation, see [14, 41, 42].

We describe the decomposition of the solution and its traction on Γ near a vertex in terms of polar coordinates (r, θ) centered at this point. Approaching the screen from the upper, respectively lower sides of the screen, we obtain the boundary values $\mathbf{u}_{\pm}$, which now involve vertex, singular and regular edge-vertex, as well as edge singularities.

$$\begin{aligned}\mathbf{u}(t,r,\theta)|_{\pm} &= C(t)\chi(r)r^{\lambda}\mathbf{\Phi}(\theta) + C_1(t)\tilde{\chi}(\theta)\boldsymbol{\beta}_1(r)(\sin(\theta))^{\frac{1}{2}} \\ &\quad + C_2(t)\tilde{\chi}(\frac{\pi}{2}-\theta)\boldsymbol{\beta}_2(r)(\cos(\theta))^{\frac{1}{2}} + \mathbf{u}_0(t,r,\theta) \\ &=: \mathbf{u}^{v} + \mathbf{u}_1^{ev} + \mathbf{u}_2^{ev} + \mathbf{u}_0. \end{aligned} \tag{3.18}$$

The corresponding decomposition of the traction is given by

$$\begin{aligned}\mathbf{p}(t,r,\theta)|_{\pm} &= C'(t)\chi(r)r^{\lambda-1}\mathbf{\Phi}'(\theta) + C_1'(t)\tilde{\chi}(\theta)\boldsymbol{\beta}_1'(r)r^{-1}(\sin(\theta))^{-\frac{1}{2}} \\ &\quad + C_2'(t)\tilde{\chi}(\frac{\pi}{2}-\theta)\boldsymbol{\beta}_2'(r)r^{-1}(\cos(\theta))^{-\frac{1}{2}} + \mathbf{w}_0(t,r,\theta) \\ &=: \mathbf{w}^{v} + \mathbf{w}_1^{ev} + \mathbf{w}_2^{ev} + \mathbf{w}_0\ . \end{aligned} \tag{3.19}$$

Here $\boldsymbol{\beta}_j(r)$ behaves like $r^{\lambda-\frac{1}{2}}$ near $r=0$, while $\boldsymbol{\beta}_j'(r)$ behaves like r^{λ}, $j=1,2$. Compared to the local coordinates near the edge in the previous section, the polar angle θ corresponds to the distance to the edge and the radius r to the variable x_3 along the edge.

For a rectangular screen $\Gamma = (0,1)\times(0,1)\times\{0\}$, the corner exponent $\lambda \simeq 0.2966$. The behavior of the corner exponent λ for a flat polygonal screen is analyzed in [43]: it is independent of material parameters, and the singularity becomes monotonically weaker, varying from r^{-1} to r^0, as the angle of the corner varies from 2π to 0.

Expansions for polyhedral domains similarly involve edge, vertex and edge-vertex singularities. The leading singular behavior near an edge coincides with that from Section 3.2. The leading singular behavior at a corner is studied, for example, in [28, 29]. The singular exponent λ is obtained as the lowest eigenvalue of a spectral problem for an elliptic operator on a spherical polygonal domain with Dirichlet boundary conditions. It generally has to be computed numerically, and we refer to [28, 29] for efficient methods.

4 | Energetic Time-Domain BIE Weak Formulation

The basic machinery for deriving a BIE formulation of equation (2.1a) is a classical one and can be found in any textbook on PDEs and boundary integral equations (see for example [44] and [45]). Hence, starting from the well known integral representation formula of the solution $\mathbf{u}(\mathbf{x};t)$ to (2.1a)

$$\mathbf{u}(\mathbf{x};t) = \mathbf{V}[\mathbf{p}(\mathbf{u})](\mathbf{x};t)\ -\mathbf{K}[\mathbf{u}](\mathbf{x};t), \qquad (\mathbf{x},t)\in\Omega\times J\ , \tag{4.1}$$

when $\mathbf{x}$ approaches the boundary Γ, $\mathbf{u}$ tends to $\overline{\mathbf{u}}$ according to the Dirichlet boundary condition in (2.1b). Consequently, with the help of a limiting process, we obtain the formulation of the elastodynamic problem as the integral equation (2.6) of the first kind on $\Gamma\times J$. Setting $\mathbf{g} := \left(\mathbf{K}+\frac{1}{2}\mathbf{I}\right)[\overline{\mathbf{u}}]$, we write this equation in the form

$$\mathbf{V}[\mathbf{w}](\mathbf{x};t) = \mathbf{g}(\mathbf{x};t), \qquad (\mathbf{x},t)\in\Gamma\times J. \tag{4.2}$$

10970207, 2025, 20, Downloaded from https://onlinelibrary.wiley.com/doi/10.1002/nme.70163 by University Degli Studi Di Messina, Wiley Online Library on [16/11/2026]. See the Terms and Conditions (https://onlinelibrary.wiley.com/terms-and-conditions) on Wiley Online Library for rules of use; OA articles are governed by the applicable Creative Commons License

Using the solution $\mathbf{w}$ from (4.2) and the Dirichlet datum, the representation formula (4.1) allows to evaluate the solution $\mathbf{u}(\mathbf{x};t)$ to the elastodynamic problem in every point of $\Omega \times J$.

For the numerical solution with a Galerkin boundary element method, we need to write (4.2) in a weak form involving suitable space-time Sobolev spaces and related norms, which are shortly recalled in Appendix A.

Having introduced the space-time bilinear form

$$\mathcal{B}_E(\mathbf{w},\mathbf{v}) = \int_0^T \int_\Gamma \mathbf{v}^\top(\mathbf{x};t)\frac{\partial}{\partial t}\mathbf{V}[\mathbf{w}](\mathbf{x};t)\mathrm{d}\Gamma_{\mathbf{x}}dt, \tag{4.3}$$

the weak formulation of (4.2) consists in finding $\mathbf{w} \in \mathrm{H}^0_\sigma(\mathbb{R}^+;\widetilde{\mathrm{H}}^{-\frac{1}{2}}(\Gamma))^3$ such that:

$$\mathcal{B}_E(\mathbf{w},\mathbf{v}) = \int_0^T \int_\Gamma \mathbf{v}^\top(\mathbf{x};t)\dot{\mathbf{g}}(\mathbf{x};t)\mathrm{d}\Gamma_{\mathbf{x}}dt \qquad \forall \mathbf{v} \in \mathrm{H}^0_\sigma(\mathbb{R}^+;\widetilde{\mathrm{H}}^{-\frac{1}{2}}(\Gamma))^3. \tag{4.4}$$

As discussed in [23], $\mathcal{B}_E$ is continuous and (weakly) coercive in the sense that

$$\|\mathbf{w}\|^2_{0,-\frac{1}{2},\Gamma,*} \leq \mathcal{B}_E(\mathbf{w},\mathbf{w}) \leq \|\mathbf{w}\|^2_{1,-\frac{1}{2},\Gamma,*}. \tag{4.5}$$

The weak boundary integral equation (4.4) for the Dirichlet problem is well-posed, due to (4.5).

Note that while the theoretical analysis requires $\sigma > 0$ on the unbounded time interval $\mathbb{R}^+$, it is common in practical computations to use $\sigma = 0$ [46].

The weak formulation (4.4) is often called energetic because it relates to the elastodynamic energy. Namely, if we choose the test function $\mathbf{v} = \mathbf{w}$, the energy balance (2.5) allows us to obtain the identity:

$$\mathcal{B}_E(\mathbf{w},\mathbf{w}) = \int_0^T \int_\Gamma \mathbf{w}^\top(\mathbf{x};t)\dot{\mathbf{g}}(\mathbf{x};t)\mathrm{d}\Gamma_{\mathbf{x}}\mathrm{d}t = \frac{1}{2}E(T) + \int_0^T \int_\Gamma \mathbf{w}^\top(\mathbf{x};t)\frac{\partial}{\partial t}\mathbf{K}[\overline{\mathbf{u}}](\mathbf{x};t)\mathrm{d}\Gamma_{\mathbf{x}}dt. \tag{4.6}$$

The bilinear form $\mathcal{B}_E(\mathbf{w},\mathbf{w})$ on the left-hand side therefore agrees with a multiple of the energy $E(T)$, up to a term which involves the Dirichlet datum.

5 | Approximation by Space-Time BEM

In order to numerically approximate the solution of the weak formulation (4.4), we introduce a space-time boundary element method. In the following we describe the Galerkin discretization of (4.4) on β-graded meshes, use the singular expansions from Section (3)to obtain quasi-optimal convergence rates and describe the algorithmic details of the proposed approach.

5.1 | Discretization

We restrict our attention to tensor product space-time discretisations of $\Sigma := \Gamma \times J$. To be specific, for the time discretization we consider a decomposition $\mathcal{T}_{\Delta_t}(J)$ of the time interval J into subintervals $J_n := [t_n, t_{n+1}]$ with constant time step $\Delta_t := T/N_{\Delta_t}$, such that $t_n := n\Delta_t$ for $n = 0, \dots, N_{\Delta_t}$.

In space we consider the approximation on quasiuniform and graded meshes $\mathcal{T}_{\Delta_x}(\Gamma) = \bigcup_{j=1}^{M_{\Delta_x}} E_j$, consisting of triangles $E_j, j = 1, \cdots, M_{\Delta_x}$. We denote by Δ_x the longest side of a triangle.

To define a β-graded mesh on the interval $[-1,1]$, for parameter $\beta > 0$, by symmetry it suffices to specify the nodes in $[-1,0]$. There we let

$$x_k = -1 + \left(\frac{k}{N_l}\right)^\beta \tag{5.1}$$

10970207, 2025, 20, Downloaded from https://onlinelibrary.wiley.com/doi/10.1002/nme.70163 by University Degli Studi Di Messina, Wiley Online Library on [16/11/2026]. See the Terms and Conditions (https://onlinelibrary.wiley.com/terms-and-conditions) on Wiley Online Library for rules of use; OA articles are governed by the applicable Creative Commons License

for $k = 1, \dots, N_l$. On the square $[-1, 1]^2$, the nodes of a β-graded mesh are given by tuples of such points, (x_k, x_l), $k, l = 1, \dots, N_l$, see Figure 2.

We refer to Section 6 for illustrations of graded meshes on more general polyhedral geometries, which are locally modeled on the previous examples. In all cases, a quasiuniform mesh is recovered for $\beta = 1$.

As explained in [5, section 7.1.3.2], following [34, section 3], a refinement of the above construction can be applied for general polyhedral domains in 3D to obtain a graded mesh on their boundary. Curved boundaries, like circular screens, are discussed in [47], see also Example 2 in Section 6 below. In the simpler case of conical singularities, one may alternatively generate nested, shape regular boundary element spaces with optimal approximation properties using local mesh refinements, following [48], as for finite element spaces in 2D polygons.

Associated to the triangulation $\mathcal{T}_{\Delta_x}(\Gamma)$, we choose a basis $\{\varphi_m\}_{m=1}^{M_{\Delta_x}}$ of Lagrangian shape functions for the space $\mathrm{X}^0_{\Delta_x}$ of piecewise constant polynomials. Similarly, for the time discretization, we fix a basis $\{\overline{\varphi}_n\}_{n=0}^{N_{\Delta_t}-1}$ of shape functions, for the space $\mathrm{X}^0_{\Delta_t}$ of piecewise constant polynomials associated to $\mathcal{T}_{\Delta_t}(J)$. Note that, in what follows, we assume:

$$\overline{\varphi}_n(t) := H(t - t_n) - H(t - t_{n+1}) \qquad \text{for} \quad n = 0, \dots, N_{\Delta_t}.$$

We define the space-time mesh $\mathcal{T}_{\Delta_x,\Delta_t}(\Sigma) := \mathcal{T}_{\Delta_t}(J) \times \mathcal{T}_{\Delta_x}(\Gamma)$. The corresponding approximation spaces are given as a tensor product of $\mathrm{X}^0_{\Delta_t}$ and $\mathrm{X}^0_{\Delta_x}$. We set $\mathbf{X}^{0,0}_{\Delta_x,\Delta_t} := \left(\mathrm{X}^0_{\Delta_t} \otimes \mathrm{X}^0_{\Delta_x}\right)^3$.

Finally, to discretize the variational formulation (4.4), we replace the unknown density field $\mathbf{w} \in \mathrm{H}^0_\sigma(\mathbb{R}^+; \mathrm{H}^{-\frac{1}{2}}(\Gamma))^3$ and the test function $\mathbf{v} \in \mathrm{H}^0_\sigma(\mathbb{R}^+; \mathrm{H}^{-\frac{1}{2}}(\Gamma))^3$ with their discrete counterparts in $\mathbf{X}^{0,0}_{\Delta_x,\Delta_t}$, respectively.

Consequently, we consider the problem of finding $\mathbf{w}_{\Delta_x,\Delta_t} \in \mathbf{X}^{0,0}_{\Delta_x,\Delta_t}$ such that:

$$\mathcal{B}_E(\mathbf{w}_{\Delta_x,\Delta_t}, \mathbf{v}_{\Delta_x,\Delta_t}) = \int_0^T \int_\Gamma \mathbf{v}^\top_{\Delta_x,\Delta_t}(\mathbf{x}; t)\dot{\mathbf{g}}(\mathbf{x}; t)\mathrm{d}\Gamma_{\mathbf{x}}\mathrm{d}t \qquad \forall \mathbf{v}_{\Delta_x,\Delta_t} \in \mathbf{X}^{0,0}_{\Delta_x,\Delta_t}. \tag{5.2}$$

From the solution $\mathbf{w}_{\Delta_x,\Delta_t}$ and the Dirichlet datum, the numerical approximations $\mathbf{u}_{\Delta_x,\Delta_t}$ to the solution of the elastodynamic problem (2.1) is obtained in $\Omega \times J$ using (4.1).

5.2 | Convergence Rates

The asymptotic expansion of the solution $\mathbf{u}$ and, more specifically, the traction $\mathbf{p}(\mathbf{u})$ on Σ, give rise to quasi-optimal convergence rates for the numerical solution of the discrete weak formulation (5.2) on graded meshes.

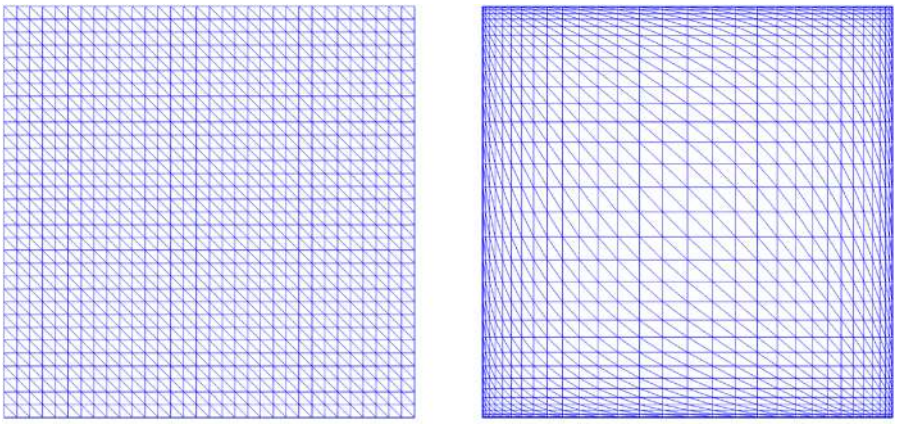

FIGURE 2 | Example 1. Meshes of Γ corresponding to $L = 16$, for $\beta = 1$ (left plot) and $\beta = 2$ (right plot).

10970207, 2025, 20, Downloaded from https://onlinelibrary.wiley.com/doi/10.1002/nme.70163 by University Degli Studi Di Messina, Wiley Online Library on [16/11/2026]. See the Terms and Conditions (https://onlinelibrary.wiley.com/terms-and-conditions) on Wiley Online Library for rules of use; OA articles are governed by the applicable Creative Commons License

For a domain in $\mathbb{R}^3$ with both wedge and cone singularities, the convergence rate will be determined by

$$\tilde{\alpha} = \min\left\{\operatorname{Re}\,\nu^*, \operatorname{Re}\,\alpha + \frac{1}{2}\right\}, \tag{5.3}$$

which depends on the geometry and the elastic parameters. Here, we recall that ν^* denotes the leading singular exponent at the edge (the minimum of $\frac{\pi}{\omega}$ and the minimal root of (3.3)), while α is the leading singular exponent at the cone tip (the leading zero of (3.14)). For a domain with only conical singularities, we set $\tilde{\alpha} = \operatorname{Re}\,\alpha + \frac{1}{2}$, while for a wedge domain in $\mathbb{R}^3$, we set $\tilde{\alpha} = \operatorname{Re}\,\nu^*$. The most singular case is given by a screen in $\mathbb{R}^3$, respectively a crack in $\mathbb{R}^2$, where in both cases $\nu^* = \frac{1}{2}$ is independent of the elastic parameters.

From [9] we recall quasi-optimal a-priori error estimates on graded meshes in these geometries:

Theorem. Let $\varepsilon > 0$ and $\sigma > 0$. Let $\mathbf{w} \in \mathrm{H}^r_\sigma(\mathbb{R}^+; \mathrm{H}^{-\frac{1}{2}}(\Gamma))^3$ be the solution to the single layer integral equation (2.6) and $\mathbf{w}_{\Delta_x,\Delta_t} \in \mathbf{X}^{0,0}_{\Delta_x,\Delta_t}$ the best approximation to $\mathbf{w}$ in the norm of $\mathrm{H}^r_\sigma(\mathbb{R}^+; \mathrm{H}^{-\frac{1}{2}}(\Gamma))^3$ on a β-graded spatial mesh with $\Delta_t \lesssim \Delta_x$. Then

$$\|\mathbf{w} - \mathbf{w}_{\Delta_x,\Delta_t}\|_{0,-\frac{1}{2},\Gamma,*} \leq C_{\beta,\varepsilon}\Delta_x^{\min\{\beta\tilde{\alpha}-\varepsilon,\frac{3}{2}\}}, \tag{5.4}$$

where $C_{\beta,\varepsilon}$ is a suitable constant depending on β, ε and $\mathbf{w}$.

In particular, for $\beta > \frac{3}{2\tilde{\alpha}}$ the convergence rate $\frac{3}{2} - \varepsilon$ gets arbitrarily close to the rate $\frac{3}{2}$ known for smooth geometries.

Corresponding convergence rates in the presence of corner singularities, as in Section 3.4, are determined by

$$\tilde{\alpha} = \min\left\{\operatorname{Re}\,\nu^*, \operatorname{Re}\,\lambda + \frac{1}{2}\right\},$$

with the corner exponent λ. We refer to [14] for a discussion in the case of the time-dependent scalar wave equation, which is readily adapted to elastodynamics.

5.3 | Algorithmic Realization

Since the unknown discrete density field $\mathbf{w}_{\Delta_x,\Delta_t}$ admits the representation

$$\mathbf{w}_{\Delta_x,\Delta_t}(\mathbf{x};t) := \sum_{n=0}^{N_{\Delta_t}-1}\overline{\varphi}_n(t)\sum_{m=1}^{M_{\Delta_x}}\mathbf{w}_m^{(n)}\varphi_m(\mathbf{x}), \qquad \mathbf{w}_m^{(n)} := \left(w_{m,1}^{(n)}, w_{m,2}^{(n)}, w_{m,3}^{(n)}\right)^\top$$

by testing equation (5.2) with basis functions, we obtain

$$\sum_{n=0}^{N_{\Delta_t}-1}\sum_{m=1}^{M_{\Delta_x}}\mathcal{B}_E(\varphi_m,\overline{\varphi}_n,\varphi_{\tilde{m}},\overline{\varphi}_{\tilde{n}})\mathbf{w}_m^{(n)} = \mathbf{g}_{\tilde{m}}^{(\tilde{n})} \qquad \text{for } \tilde{m} = 1,\dots,M_{\Delta_x},\ \tilde{n} = 1,\dots,N_{\Delta_t}$$

where

$$\mathcal{B}_E(\varphi_m,\overline{\varphi}_n,\varphi_{\tilde{m}},\overline{\varphi}_{\tilde{n}}) = -\int_0^T\int_\Gamma\left(\int_0^t\int_\Gamma \mathbf{G}(\mathbf{x},\mathbf{y};t,\tau)\varphi_m(\mathbf{y})\overline{\varphi}_n(\tau)\mathrm{d}\Gamma_\mathbf{y}\mathrm{d}\tau\right)\varphi_{\tilde{m}}(\mathbf{x})\dot{\overline{\varphi}}_{\tilde{n}}(t)\mathrm{d}\Gamma_\mathbf{x}\mathrm{d}t$$

and

$$\mathbf{g}_{\tilde{m}}^{(\tilde{n})} = -\int_0^T\int_\Gamma \mathbf{g}(\mathbf{x};t)\varphi_{\tilde{m}}(\mathbf{x})\dot{\overline{\varphi}}_{\tilde{n}}(t)\mathrm{d}\Gamma_\mathbf{x}\mathrm{d}t\ .$$

We focus our attention on $\mathcal{B}_E(\varphi_m,\overline{\varphi}_n,\varphi_{\tilde{m}},\overline{\varphi}_{\tilde{n}})$. As the fundamental solution depends only on the difference $t-\tau$ and the considered decomposition of the time interval is uniform, the temporal integrals depend only on the difference $\Delta_{\tilde{n},n} :=$

10970207, 2025, 20, Downloaded from https://onlinelibrary.wiley.com/doi/10.1002/nme.70163 by University Degli Studi Di Messina, Wiley Online Library on [16/11/2026]. See the Terms and Conditions (https://onlinelibrary.wiley.com/terms-and-conditions) on Wiley Online Library for rules of use; OA articles are governed by the applicable Creative Commons License

$t_{\tilde{n}} - t_n$ and in particular they vanish if $t_{\tilde{n}} < t_n$. Thus, the duality pairing with all the basis functions leads to the block lower triangular Toeplitz system

$$\begin{pmatrix} \mathbb{E}^{(0)} & 0 & 0 & 0 & 0 \\ \mathbb{E}^{(1)} & \mathbb{E}^{(0)} & 0 & 0 & 0 \\ \mathbb{E}^{(2)} & \mathbb{E}^{(1)} & \mathbb{E}^{(0)} & 0 & 0 \\ \vdots & \vdots & \vdots & \ddots & \vdots \\ \mathbb{E}^{(N_{\Delta_t}-1)} & \mathbb{E}^{(N_{\Delta_t}-2)} & \mathbb{E}^{(N_{\Delta_t}-3)} & \dots & \mathbb{E}^{(0)} \end{pmatrix} \begin{pmatrix} \mathbf{w}^{(1)} \\ \mathbf{w}^{(2)} \\ \mathbf{w}^{(3)} \\ \vdots \\ \mathbf{w}^{(N_{\Delta_t}-1)} \end{pmatrix} = \begin{pmatrix} \mathbf{g}^{(1)} \\ \mathbf{g}^{(2)} \\ \mathbf{g}^{(3)} \\ \vdots \\ \mathbf{g}^{(N_{\Delta_t}-1)} \end{pmatrix} \tag{5.5}$$

where, for each $\ell = \tilde{n} - n = 0, \dots, N_{\Delta_t} - 1$, the block $\mathbb{E}^{(\ell)}$ is a $3M_{\Delta_x}$-by-$3M_{\Delta_x}$ matrix, because each pair of spatial indices $\tilde{m}, m = 1, \dots, M_{\Delta_x}$ does not define a single entry but rather a 3-by-3 subblock, that is,

$$\left(\mathbb{E}^{(\ell)}_{\tilde{m},m}\right)_{ij} = -\int_0^T \int_\Gamma \left(\int_0^t \int_\Gamma G_{ij}(\mathbf{x}, \mathbf{y}; t, \tau) \varphi_m(\mathbf{y}) \overline{\varphi}_n(\tau) \mathrm{d}\Gamma_{\mathbf{y}} \mathrm{d}\tau \right) \varphi_{\tilde{m}}(\mathbf{x}) \dot{\overline{\varphi}}_{\tilde{n}}(t) \mathrm{d}\Gamma_{\mathbf{x}} \mathrm{d}t \tag{5.6}$$

A main challenge of the energetic BEM is the accurate and efficient evaluation of the quadruple integrals in (5.6). After a double analytic integration in the time variables, we obtain:

$$\left(\mathbb{E}^{(\ell)}_{\tilde{m},m}\right)_{ij} = -\frac{1}{4\pi\varrho} \sum_{\eta,\tilde{\eta}=0}^{1} (-1)^{\eta+\tilde{\eta}} \int_\Gamma \int_\Gamma \mathbb{G}_{ij}(\mathbf{x}, \mathbf{y}; \Delta_{\tilde{n}+\tilde{\eta},n+\eta}) \varphi_m(\mathbf{y}) \varphi_{\tilde{m}}(\mathbf{x}) \mathrm{d}\Gamma_{\mathbf{y}} \mathrm{d}\Gamma_{\mathbf{x}}, \tag{5.7}$$

where the components of the time-integrated kernel $\mathbb{G}$ are given by

$$\begin{aligned} \mathbb{G}_{ij}(\mathbf{x}, \mathbf{y}; \Delta_{\tilde{n},n}) = {} & \frac{1}{c_{\mathrm{P}}^2} \frac{r_i r_j}{r^3} H\left(\Delta_{\tilde{n},n} - \frac{r}{c_{\mathrm{P}}}\right) + \frac{1}{c_{\mathrm{S}}^2} \left(\frac{\delta_{ij}}{r} - \frac{r_i r_j}{r^3}\right) H\left(\Delta_{\tilde{n},n} - \frac{r}{c_{\mathrm{S}}}\right) + \\ & - \frac{1}{2} \left(\frac{\delta_{ij}}{r^3} - \frac{r_i r_j}{r^5}\right) \left[\left(\Delta_{\tilde{n},n}^2 - \frac{r^2}{c_{\mathrm{P}}^2}\right) H\left(\Delta_{\tilde{n},n} - \frac{r}{c_{\mathrm{P}}}\right) - \left(\Delta_{\tilde{n},n}^2 - \frac{r^2}{c_{\mathrm{S}}^2}\right) H\left(\Delta_{\tilde{n},n} - \frac{r}{c_{\mathrm{S}}}\right) \right] \end{aligned} \tag{5.8}$$

In the above relationship, the Heaviside functions represent the wave front propagation and their contribution is 0 or 1. If $r < c_{\mathrm{S}}\Delta_{\tilde{n},n} < c_{\mathrm{P}}\Delta_{\tilde{n},n}$, then (5.8) reduces to

$$\mathbb{G}_{ij}(\mathbf{x}, \mathbf{y}; \Delta_{\tilde{n},n}) = \frac{1}{2} \left(\frac{r_i r_j}{r^3} \frac{c_{\mathrm{P}}^2 - c_{\mathrm{S}}^2}{c_{\mathrm{P}}^2 c_{\mathrm{S}}^2} + \frac{\delta_{ij}}{r} \frac{c_{\mathrm{P}}^2 + c_{\mathrm{S}}^2}{c_{\mathrm{P}}^2 c_{\mathrm{S}}^2} \right) \tag{5.9}$$

and we observe a space singularity of type $\mathcal{O}(\frac{1}{r})$ as $r \to 0$, which is typical of weakly singular kernels related to 3D elliptic problems. Moreover, when $0 < c_{\mathrm{S}}\Delta_{\tilde{n},n} < r < c_{\mathrm{P}}\Delta_{\tilde{n},n}$, (5.8) is no longer singular and becomes

$$\mathbb{G}_{ij}(\mathbf{x}, \mathbf{y}; \Delta_{\tilde{n},n}) = \frac{1}{2} \left(\frac{1}{c_{\mathrm{P}}^2} \frac{\delta_{ij}}{r} - \frac{1}{c_{\mathrm{P}}^2} \frac{r_i r_j}{r^3} - \frac{\delta_{ij}}{r^3} \Delta_{\tilde{n},n}^2 + 3 \frac{r_i r_j}{r^5} \Delta_{\tilde{n},n}^2 \right). \tag{5.10}$$

For what concerns the double integration in space variables, we remember that we are considering lagrangian piecewise constant basis and test functions. Consequently, we can reduce the integrals over Γ to double integrals over the source and the field triangles $E_{\tilde{m}}$ and E_m respectively. Thus, we consider

$$\left(\mathbb{E}^{(\ell)}_{\tilde{m},m}\right)_{ij} = -\frac{1}{4\pi\varrho} \sum_{\eta,\tilde{\eta}=0}^{1} (-1)^{\eta+\tilde{\eta}} \int_{E_{\tilde{m}}} \int_{E_m} \mathbb{G}_{ij}(\mathbf{x}, \mathbf{y}; \Delta_{\tilde{n}+\tilde{\eta},n+\eta}) \mathrm{d}\Gamma_{\mathbf{y}} \mathrm{d}\Gamma_{\mathbf{x}} \tag{5.11}$$

and we carry out the outer integration on the source triangle by applying a M_g-point suitable quadrature rule, so that

$$\left(\mathbb{E}^{(\ell)}_{\tilde{m},m}\right)_{ij} \simeq -\frac{1}{4\pi\varrho} \sum_{\eta,\tilde{\eta}=0}^{1} (-1)^{\eta+\tilde{\eta}} \sum_{q=1}^{M_g} \omega_q \int_{E_m} \mathbb{G}_{ij}(\mathbf{x}_q, \mathbf{y}; \Delta_{\tilde{n}+\tilde{\eta},n+\eta}) \mathrm{d}\Gamma_{\mathbf{y}}, \tag{5.12}$$

10970207, 2025, 20, Downloaded from https://onlinelibrary.wiley.com/doi/10.1002/nme.70163 by University Degli Studi Di Messina, Wiley Online Library on [16/11/2026]. See the Terms and Conditions (https://onlinelibrary.wiley.com/terms-and-conditions) on Wiley Online Library for rules of use; OA articles are governed by the applicable Creative Commons License

where $\mathbf{x}_q$ and ω_q are the quadrature nodes and weights, respectively. The remaining integral requires integration over geometrically complicated intersections of the field triangle with two spherical surfaces of radii $r_P = c_P\Delta_{\tilde{n},n}$ and $r_S = c_S\Delta_{\tilde{n},n}$, representing the wave fronts of the P- and S-waves. To address this issue, we project the source point $\mathbf{x}_q$ onto the field triangle plane and we use a careful decomposition of the area of integration into sample standard shapes in polar coordinates. Thus, the integration is performed analytically, as described in [23].

To evaluate the right-hand side of system (5.5) for a datum $\mathbf{g}(\mathbf{x};t)$ given in closed form, as we have considered in the numerical simulations below, we apply standard Gaussian quadrature rules. Otherwise, for the numerical treatment of the integral operator $\mathbf{K}$ the interested reader is referred to [49].

Finally, the space-time system (5.5) may be solved by a block forward substitution, that leads to a marching-on-in-time time stepping scheme. This scheme is proved to be unconditionally stable and first-order accurate in Δ_t for 3D scalar problems in the framework of an energetic BEM-FEM coupling [50]. Therefore, under the assumption that the matrix $(\mathbb{E}^{(0)}$ is non singular, which is confirmed by all the numerical testing that has been performed on the energetic approach, at every time instant t_ℓ with $\ell = 0, \dots, N_{\Delta_t} - 1$, one has to solve the reduced linear system

$$(\mathbb{E}^{(0)}\mathbf{w}^{(\ell)} = \mathbf{g}^{(\ell)} - \sum_{k=0}^{\ell-1}(\mathbb{E}^{(\ell-k)}\mathbf{w}^{(k)}.$$

We remark that blocks $(\mathbb{E}^{(\ell)}$, with $\ell = 1, \dots, N_{\Delta_t} - 1$, are only used to update at every time step the right-hand side. For this reason the LU factorization on the block $(\mathbb{E}^{(0)}$ needs to be performed and stored only once at the beginning of the time stepping scheme.

6 | Numerical Results

In this section we present numerical experiments which validate the convergence properties of the proposed approach and study the singular behavior of the solution. We first discuss computational aspects common to all the experiments.

For the numerical evaluation of integrals that define the entries $(\mathbb{E}^{(\ell)}_{\tilde{m},m}$ in (5.12), we have applied a quadrature rule with M_g nodes and weights, obtained with the algorithm described in [51]. The choices $M_g = 7$ for the first three examples, $M_g = 12$ for the fourth example and $M_g = 19$ for the last example have guaranteed the computation of the mentioned integrals with a sufficiently high accuracy. This is a key issue to assure the convergence and space-time accuracy of the energetic BEM in the context of 3D elastodynamic problems, whose theoretical analysis been performed in [9].

All the numerical computations have been performed on a cluster with two Intel XEON E5-2683v4 CPUs (2.1 GHz clock frequency and 16 cores) by means of parallel MATLAB codes.

A natural measure of the error relies on the (squared) energy, which is defined from the identity (4.6) and computed in the discrete framework from the matrix ($\mathbb{E}$ or the right hand side vector $\mathbf{g}$ and the solution vector $\mathbf{w}$ as

$$\mathcal{E}(\mathbf{w}) := \mathbf{w}^\top(\mathbb{E}\mathbf{w} = \mathbf{w}^\top\mathbf{g}. \tag{6.1}$$

We compute the squared energy error with respect to an extrapolated benchmark energy $\mathcal{E}_\infty$ as

$$\mathrm{Err}_L := \mathcal{E}_\infty - \mathcal{E}(\mathbf{w}_L) \tag{6.2}$$

where the subscript L refers to the refinement level.

In the first two examples, we study the numerical solution of the integral equation (4.2) on a flat screen Γ using the Galerkin formulation (5.2) and considering the datum $\mathbf{g}(\mathbf{x};t) = \left(0, 0, x_1^2\sin^5 t\right)^\top$. The final time is set as $T = 1$, while the material parameters $\rho = 1$, $\mu = 0.25$ and $\lambda = 0.5$ are taken in such a way that $c_P = 1$, $c_S = 0.5$, unless otherwise stated.

On the screen Γ we introduce an algebraically graded mesh, whose construction on a general polyhedral surface is described in [34]. In what follows, $\beta \geq 1$ is the grading parameter of the mesh, and the level $L \geq 1$ relates to the (square root of the) number of triangles on Γ. To study the convergence, we start by choosing a coarse mesh associated to the value $L = 2$ and successively double the value of L.

10970207, 2025, 20, Downloaded from https://onlinelibrary.wiley.com/doi/10.1002/nme.70163 by University Degli Studi Di Messina, Wiley Online Library on [16/11/2026]. See the Terms and Conditions (https://onlinelibrary.wiley.com/terms-and-conditions) on Wiley Online Library for rules of use; OA articles are governed by the applicable Creative Commons License

Example 1 (Square screen). We consider $\Gamma := [-\ell, \ell]^2 \times \{x_3 = 0\}$, with $\ell = 0.5$. Due to its symmetry with respect to the origin, the β-graded space mesh is generated on the bottom-left quarter of Γ by the nodes $(x_{1,k}^{(L)}, x_{2,k}^{(L)})$, where

$$x_{1,k}^{(L)} = \ell\left(-1 + \left(\frac{k}{L}\right)^{\beta}\right) \qquad \text{and} \qquad x_{2,h}^{(L)} = \ell\left(-1 + \left(\frac{h}{L}\right)^{\beta}\right), \qquad \text{for} \quad k, h = 0, \dots, L\,,$$

which have been then reflected to obtain a mesh on the whole screen. The total number of triangles is proportional to L^2.

Note that the parameter $\Delta_{\mathbf{x}}$ is proportional to $\ell_{\max} := \ell[1 - (1 - 1/L)^{\beta}]$, while the parameter $\ell_{\min} := \ell L^{-\beta}$ is related to the smallest element of the mesh. For uniform meshes, that is, for $\beta = 1$, it is easy to see that $\ell_{\max} = \ell_{\min} = \ell/L$. In Table 1, we report the space-time discretization parameters, associated to the decomposition of the computational domain for $\beta = 1, 2$.

In Figure 2 the meshes corresponding to the $L = 16$ are represented for $\beta = 1$ (left plot) and $\beta = 2$ (right plot).

Figure 3 shows the component in the x_3-direction of the numerical solution $\mathbf{w}_{\Delta_{\mathbf{x}},\Delta_t}$ (the only non-trivial one) on Γ in the scaled left plot and along a cross-section in the right plot at the final time. Here, a 2-graded mesh with $L = 32$ was used.

Moreover, the asymptotic behavior of the numerical solutions for $\beta = 1, 2$, $L = 32$, at $T = 1$, is shown in Figure 4, along the x_1-axis, for $x_2 = x_3 = 0$. Here, the horizontal axis uses the distance r from the left side of the screen. The singular behavior of the numerical solution on the 2-graded mesh (green line), respectively, on the uniform mesh (blue line), agrees with the theoretically predicted behavior from Section 3.4, that is, $\mathcal{O}(r^{-1/2})$ (dashed red line).

In Figure 5 we depict the asymptotic behavior of the numerical solution at $T = 1$ for different ratios between primary and secondary wave speeds, again for $\beta = 2$ and $L = 32$. The left plot depicts the numerical solution along the x_1-axis with respect to the distance r from the left side of the screen. The behavior $O(r^{-0.5})$ is independent of the elastodynamic parameters, as theoretically discussed in Section 3.4. Similarly, the right plot depicts the numerical solution along the line $x_2 = -x_1$ with respect to the distance from the top-left corner. The singular behavior $O(r^{-0.78})$ is independent of the

TABLE 1 | Example 1. Discretization parameters of the square screen β-meshes with $\beta = 1$ and $\beta = 2$, for different values of L.

L	Δ_t	N_{Δ_t}	$\ell_{\max} = \ell_{\min}$ $(\beta = 1)$	$\ell_{\max}$ $(\beta = 2)$	$\ell_{\min}$ $(\beta = 2)$	$M_{\Delta_{\mathbf{x}}}$
2	$2.5000e-01$	4	$2.5000e-01$	3.7500e-01	$1.2500e-01$	32
4	$1.2500e-01$	8	$1.2500e-01$	2.1875e-01	$3.1250e-02$	128
8	$6.2500e-02$	16	$6.2500e-02$	1.1719e-01	$7.8125e-03$	512
16	$3.1250e-02$	32	$3.1250e-02$	6.0547e-02	$1.9531e-03$	2048
32	$1.5625e-02$	64	$1.5625e-02$	3.0762e-02	$4.8828e-04$	8192

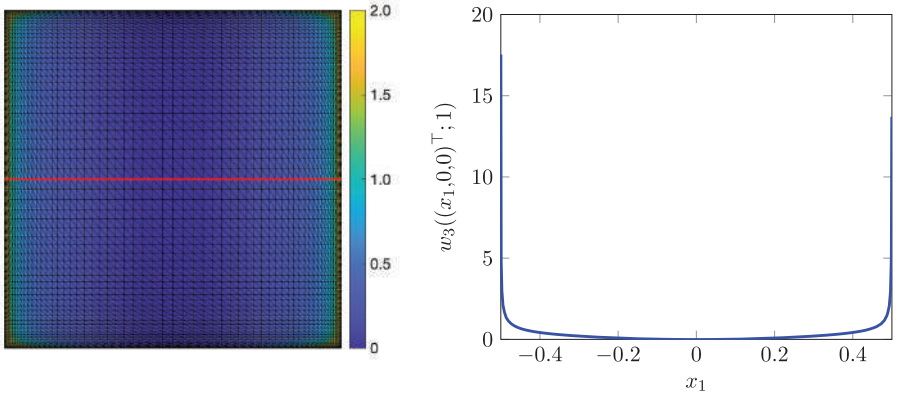

FIGURE 3 | Example 1. For the β-graded mesh with $\beta = 2$ and $L = 32$, component in x_3-direction of the numerical solution $\mathbf{w}_{\Delta_{\mathbf{x}},\Delta_t}$ at the final time $T = 1$ on Γ (scaled left plot) and along $x_2 = 0$ (right plot).

10970207, 2025, 20, Downloaded from https://onlinelibrary.wiley.com/doi/10.1002/nme.70163 by University Degli Studi Di Messina, Wiley Online Library on [16/11/2026]. See the Terms and Conditions (https://onlinelibrary.wiley.com/terms-and-conditions) on Wiley Online Library for rules of use; OA articles are governed by the applicable Creative Commons License

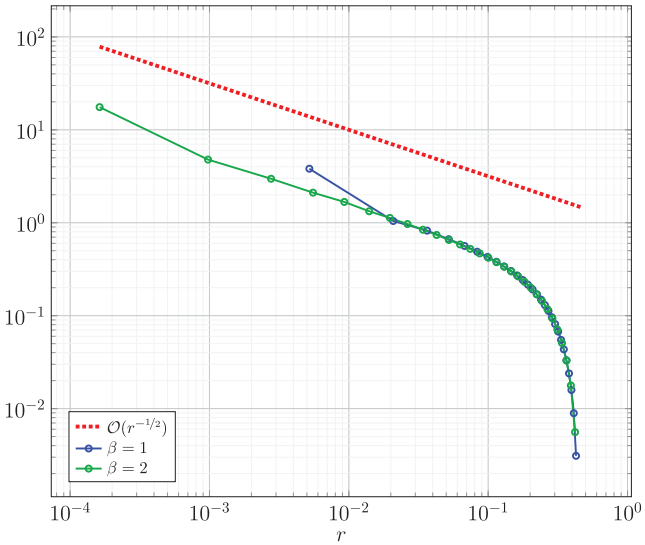

FIGURE 4 | Example 1. Asymptotic behavior of the numerical solution ($L = 32$) along the x_1-axis, at $T = 1$, for $\beta = 1, 2$. The plot is with respect to the distance r from the left side of the screen.

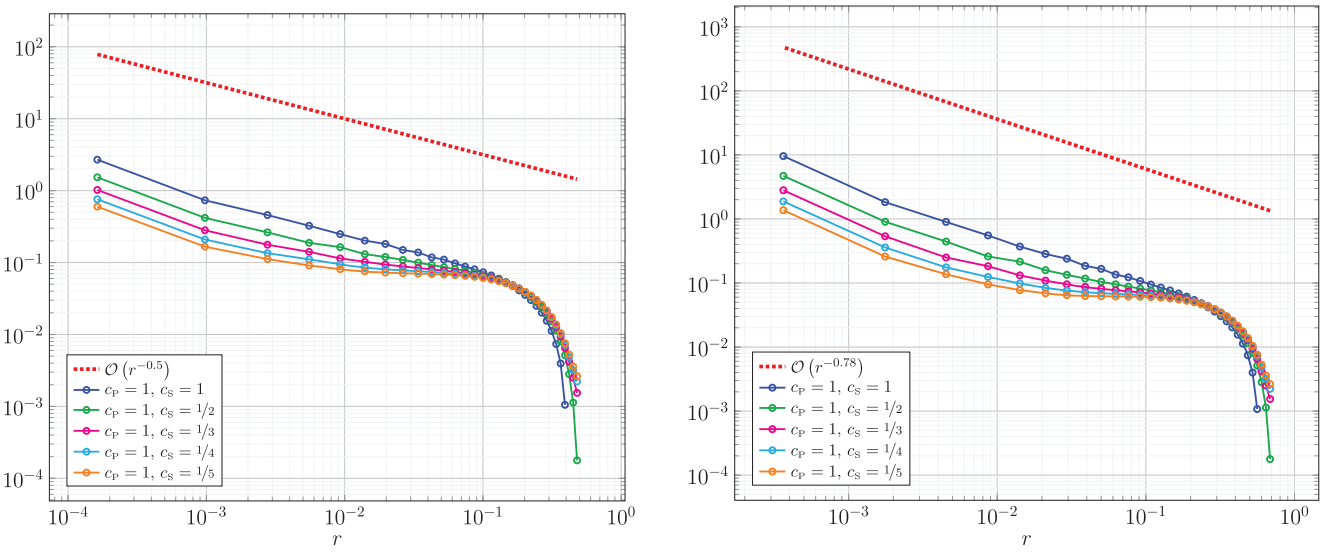

FIGURE 5 | Example 1. Asymptotic behavior of the numerical solution ($L = 32$) along the x_1-axis (left plot) and along the line $x_2 = -x_1$ (right plot), at $T = 1$, for $\beta = 2$ and different ratios between primary and secondary wave speeds. The plot is with respect to the distance r from the screen boundary.

elastodynamic parameters and in line with the theoretical analysis in Section 3.4. The qualitative behavior agrees with that obtained for the scalar wave equation in [14].

In Table 2 we report the values of the squared energy $\mathcal{E}_L := \mathcal{E}(\mathbf{w}_L)$ of the numerical solution. Figure 6 presents the squared energy errors with respect to the common benchmark $\mathcal{E}_\infty = 0.0145377$, which was obtained by extrapolation from the energy values for $\beta = 2$. The convergence rate $\simeq \beta$ is in very good agreement with the theoretical prediction from Section 5.2.

Let us remark that to reach an accuracy level of $O(10^{-2})$ we need 524.288 space-time DoFs using a uniform mesh, that is, $\beta = 1$, while we need only 1028 space-time DoFs using a graded mesh with $\beta = 2$. This highlights the computational and memory savings from using graded meshes. Corresponding to the higher convergence rate on β-graded meshes, the savings increase for higher accuracy, as can be deduced from the horizontal separation of the lines in Figure 6. Analogously, increasing computational savings at higher accuracies are observed in all the examples below.

10970207, 2025, 20, Downloaded from https://onlinelibrary.wiley.com/doi/10.1002/nme.70163 by University Degli Studi Di Messina, Wiley Online Library on [16/11/2026]. See the Terms and Conditions (https://onlinelibrary.wiley.com/terms-and-conditions) on Wiley Online Library for rules of use; OA articles are governed by the applicable Creative Commons License

TABLE 2 | Example 1. Squared energy values of the numerical solution at $T = 1$ for $\beta = 1, 2$ and different values of L.

L	2	4	8	16	32
$\mathcal{E}_L$ $(\beta = 1)$	$1.1518e-02$	$1.3088e-02$	$1.3804e-02$	$1.4162e-02$	$1.4345e-02$
$\mathcal{E}_L$ $(\beta = 2)$	$1.2867e-02$	$1.4197e-02$	$1.4458e-02$	$1.4519e-02$	$1.4533e-02$

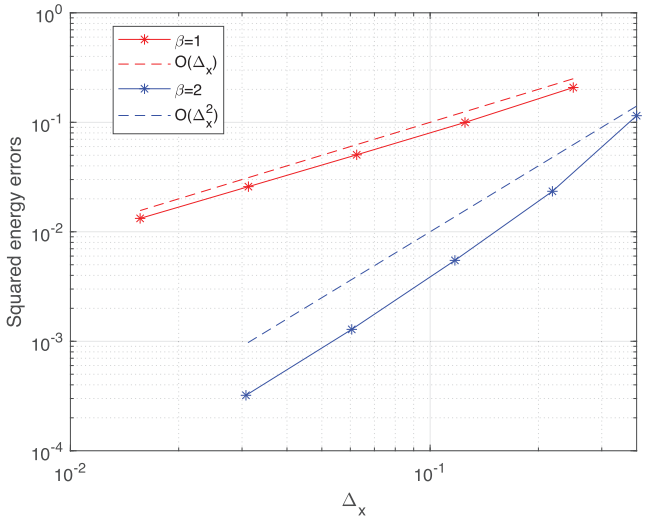

FIGURE 6 | Example 1. Squared errors in energy norm for $[\beta = 1, \beta = 2]$.

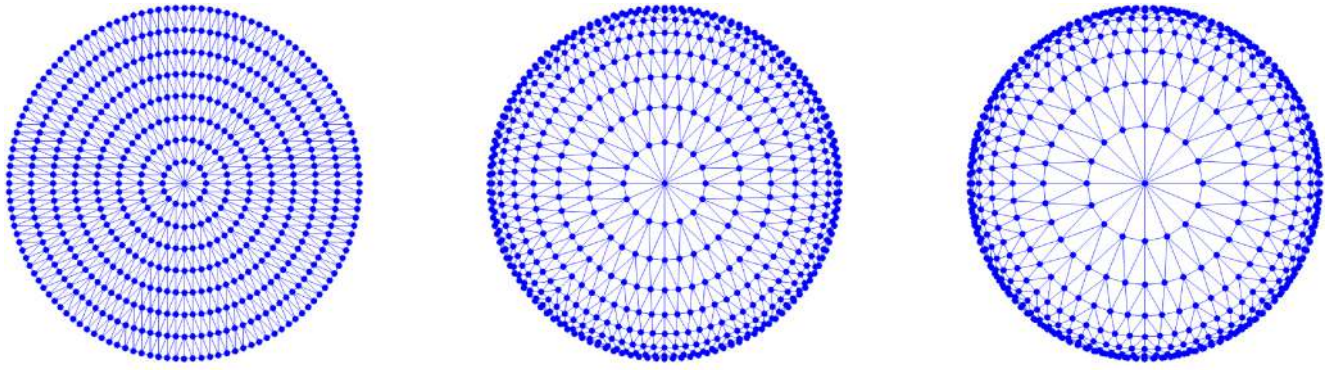

FIGURE 7 | Example 2. Meshes of Γ corresponding to $L = 8$, for $\beta = 1$ (left plot), $\beta = 2$ (center plot) and $\beta = 3$ (right plot).

Example 2 (Circular screen). We consider $\Gamma := \{x_1^2 + x_2^2 \leq R^2\} \times \{x_3 = 0\}$, with $R = 0.5$. Following [52], the radial coordinates of the nodes of the β-graded mesh are given by $r_k = R\left(1 - (\frac{k}{L})^\beta\right)$, $k = 0, \ldots, L$, while the angular coordinates of the nodes on each internal circle of radius r_k are $\theta_i^{(k)} = \frac{\pi}{kL} i$, $i = 1, \ldots, 2kL$. This means that the number of angular elements is increased towards the boundary as shown in Figure 7, where the meshes corresponding to $L = 8$ are represented for $\beta = 1$ (left plot), $\beta = 2$ (center plot) and $\beta = 3$ (right plot). For $\beta = 1$ a quasi-uniform mesh is obtained.

The parameters $\ell_{\max}$ and $\ell_{\min}$ for $\beta = 1, 2$ are the same as in Table 1, while for $\beta = 3$ they are shown in Table 3, together with the remaining discretization parameters.

Figure 8 shows the component in x_3-direction of the numerical solution $\mathbf{w}_{\Delta_x, \Delta_t}$ (the only one not trivial) on Γ (scaled left plot) and along a cross-section (right plot) at the final time. These results are obtained by considering a β-graded mesh with $\beta = 3$ for $L = 16$.

10970207, 2025, 20, Downloaded from https://onlinelibrary.wiley.com/doi/10.1002/nme.70163 by University Degli Studi Di Messina, Wiley Online Library on [16/11/2026]. See the Terms and Conditions (https://onlinelibrary.wiley.com/terms-and-conditions) on Wiley Online Library for rules of use; OA articles are governed by the applicable Creative Commons License

TABLE 3 | Example 2. Discretization parameters of the circular screen β-mesh with $\beta = 3$. for different values of L.

L	Δ_t	N_{Δ_t}	$\ell_{\max}$ $(\beta = 3)$	$\ell_{\min}$ $(\beta = 3)$	M_{Δ_x}
2	$2.5000e-01$	4	$4.3750e-01$	$6.2500e-02$	16
4	$1.2500e-01$	8	$2.8906e-01$	$7.8125e-03$	128
8	$6.2500e-02$	16	$1.6504e-01$	$9.7656e-04$	1024
16	$3.1250e-02$	32	$8.8013e-02$	$1.2207e-04$	8192

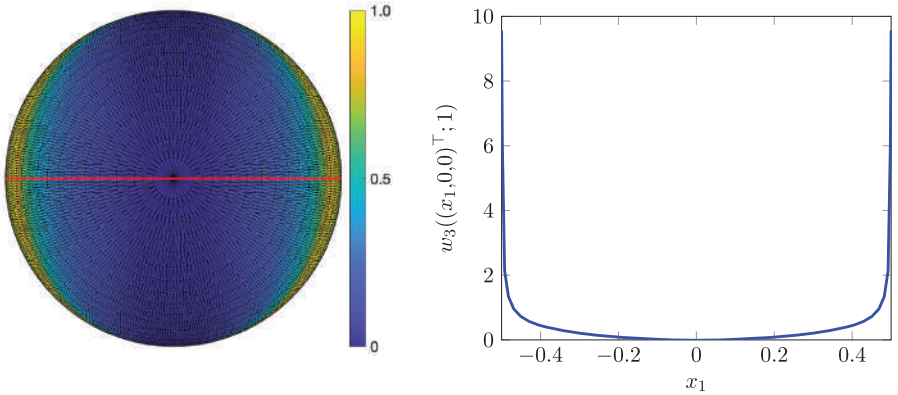

FIGURE 8 | Example 2. For the β-graded mesh with $\beta = 3$ and $L = 16$, component in x_3-direction of the numerical solution $\mathbf{w}_{\Delta_x,\Delta_t}$ at the final time $T = 1$ on Γ (scaled left plot) and along $x_2 = 0$ (right plot).

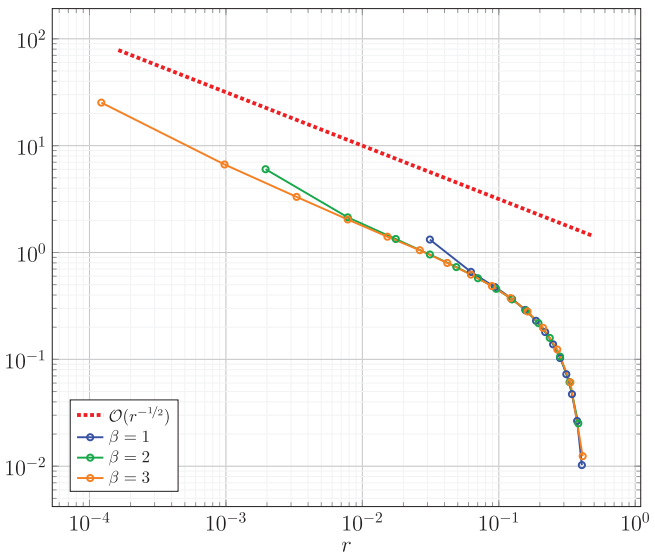

FIGURE 9 | Example 2. Asymptotic behavior of the numerical solution $(L = 16)$ along the (x_1)-axis, at $(T = 1)$, for $(\beta = 1, 2, 3)$. The plot is with respect to the distance (r) from the circular screen boundary.

Figure 9 shows the asymptotic behavior of the numerical solutions at $T = 1$ along the x_1-axis, for $x_2 = x_3 = 0$, with respect to the distance r from the boundary of the circular screen. Here, $\beta = 1, 2, 3$, $L = 16$, have been used. The singular behavior of the numerical solutions agrees with the theoretically predicted behavior from Section 3.4, that is, $\mathcal{O}(r^{-1/2})$ (dashed red line), particularly for $\beta = 3$.

In Table 4 we report the values of the squared energy $\mathcal{E}_L$ of the numerical solution. Figure 10 presents the squared energy errors with respect to the common benchmark $\mathcal{E}_\infty = 0.0071888$, which was obtained by extrapolation from the energy values for $\beta = 3$. Again, the convergence rate $\simeq \beta$ is in very good agreement with the theoretical prediction from Section 5.2.

10970207, 2025, 20, Downloaded from https://onlinelibrary.wiley.com/doi/10.1002/nme.70163 by University Degli Studi Di Messina, Wiley Online Library on [16/11/2026]. See the Terms and Conditions (https://onlinelibrary.wiley.com/terms-and-conditions) on Wiley Online Library for rules of use; OA articles are governed by the applicable Creative Commons License

TABLE 4 | Example 2. Squared energy values of the numerical solution at $T = 1$ for $\beta = 1, 2, 3$ and different values of L.

L	2	4	6	8	12	16
$\mathcal{E}_L$ ($\beta = 1$)	$4.0000e-03$	$6.3122e-03$	$6.7169e-03$	$6.8562e-03$	$6.9901e-03$	$7.0454e-03$
$\mathcal{E}_L$ ($\beta = 2$)	$4.6143e-03$	$6.8793e-03$	$7.0906e-03$	$7.1386e-03$	$7.1679e-03$	$7.1751e-03$
$\mathcal{E}_L$ ($\beta = 3$)	$4.8380e-03$	$7.0302e-03$	$7.1698e-03$	$7.1860e-03$	$7.1880e-03$	$7.1885e-03$

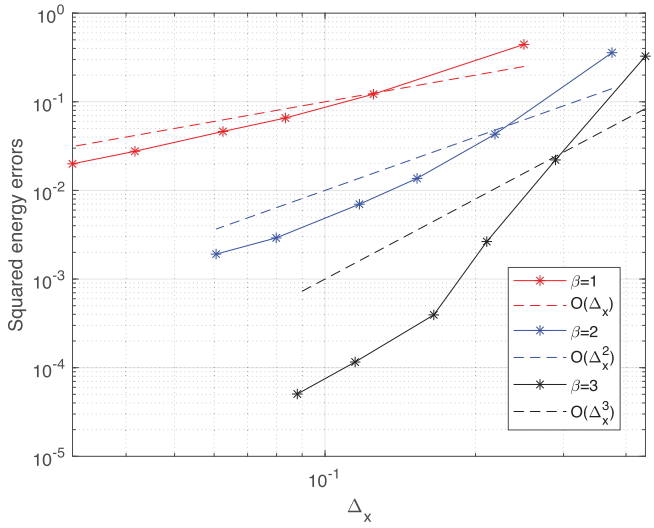

FIGURE 10 | Example 2. Squared errors in energy norm for $\beta = 1, 2, 3$.

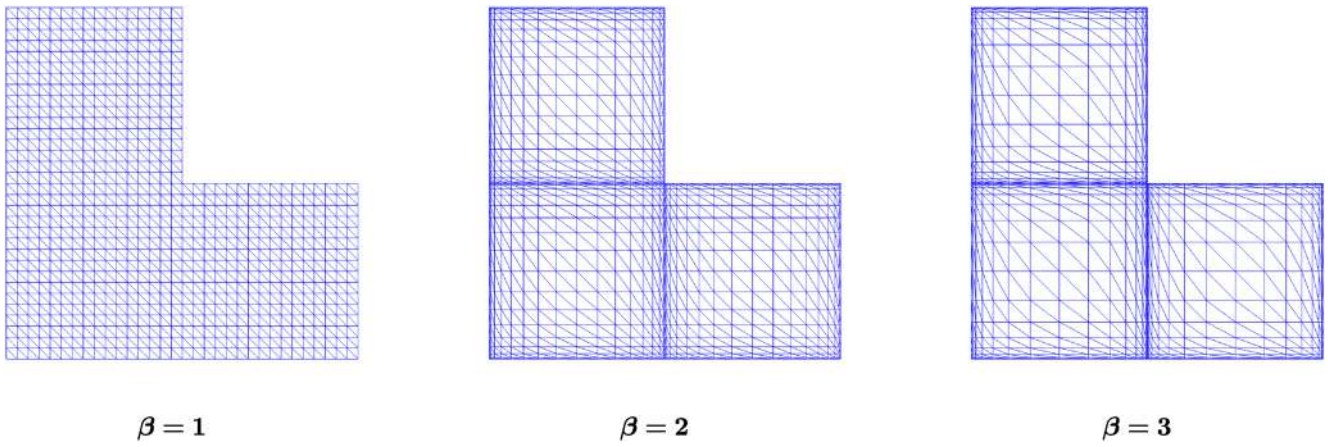

FIGURE 11 | Example 3. Meshes of Γ corresponding to $L = 16$, for $\beta = 1$ (left plot), $\beta = 2$ (center plot) and $\beta = 3$ (right plot).

To conclude, we observe that to reach an accuracy level of $O(10^{-2})$ we need 262.144 space-time DoFs using a uniform mesh, that is, $\beta = 1$, while we need 5.184 space-time DoFs using a graded mesh with $\beta = 2$ and only 1024 space-time DoFs using a graded mesh with $\beta = 3$.

Example 3 (L-shaped screen). In this example, we consider $\Gamma := ([-\ell, \ell]^2 \setminus [0, \ell]^2) \times \{x_3 = 0\}$, with $\ell = 0.5$, and the datum $\mathbf{g}(\mathbf{x}; t) = \left(0, 0, [(x_1 + \ell)^2 + (x_2 + \ell)^2]\sin^5 t\right)^{\mathsf{T}}$. The final time is set $T = 1$, while the material parameters $\rho = 1$, $\mu = 0.25$ and $\lambda = 0.5$ are taken, in such a way that $c_{\mathrm{P}} = 1$, $c_{\mathrm{S}} = 0.5$.

The graded mesh on the L-shape is obtained from three copies of the graded mesh used in Example 1, see Figure 11 for the meshes corresponding to $L = 16$ with $\beta = 1$ (left plot), $\beta = 2$ (center plot) and $\beta = 3$ (right plot). The discretization parameters for $\beta = 1, 2$ are shown in Table 5.

10970207, 2025, 20, Downloaded from https://onlinelibrary.wiley.com/doi/10.1002/nme.70163 by University Degli Studi Di Messina, Wiley Online Library on [16/11/2026]. See the Terms and Conditions (https://onlinelibrary.wiley.com/terms-and-conditions) on Wiley Online Library for rules of use; OA articles are governed by the applicable Creative Commons License

TABLE 5 | Example 3. Discretization parameters of the L-shaped screen β-meshes with $\beta = 1$ and $\beta = 2$, for different values of L.

L	Δ_t	N_{Δ_t}	$\ell_{\max} = \ell_{\min}$ $(\beta = 1)$	$\ell_{\max}$ $(\beta = 2)$	$\ell_{\min}$ $(\beta = 2)$	M_{Δ_x}
2	$1.2500e-01$	8	$1.2500e-01$	$1.8750e-01$	$6.2500e-02$	96
4	$6.2500e-02$	16	$6.2500e-02$	$1.0938e-01$	$1.5625e-02$	384
8	$3.1250e-02$	32	$3.1250e-02$	$5.8594e-02$	$3.9062e-03$	1536
16	$1.5625e-02$	64	$1.5625e-02$	$3.0273e-02$	$9.7656e-04$	6144

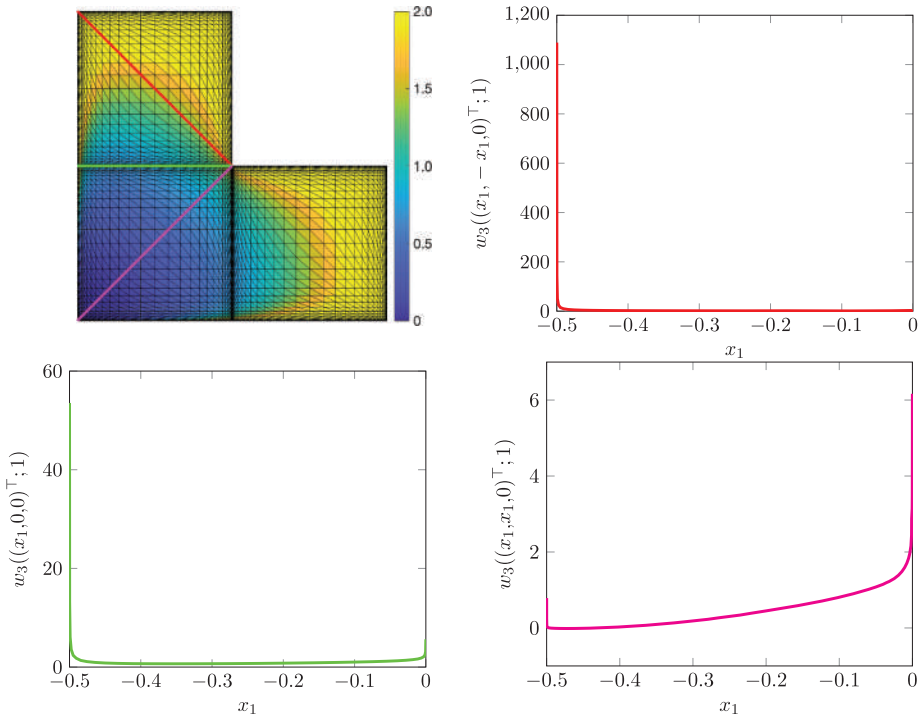

FIGURE 12 | Example 3. For the β-graded mesh with $\beta = 3$ and $L = 16$, component in x_3-direction of the numerical solution $\mathbf{w}_{\Delta_x,\Delta_t}$ at the final time $T = 1$ on Γ (scaled left-top plot) and along three cross-sections (right-top plot along the red diagonal, left-bottom plot along the green segment on the x_1 axis, right-bottom plot along the magenta diagonal).

Figure 12 shows the component in x_3-direction of the numerical solution $\mathbf{w}_{\Delta_x,\Delta_t}$ (the only one not trivial) on Γ (scaled left-top plot) and along three cross-sections (right-top plot along the red diagonal, left-bottom plot along the green segment on the x_1 axis, right-bottom plot along the magenta diagonal) at the final time. These results are obtained on a β-graded mesh with $\beta = 3$ for $L = 16$. We observe the singular behavior of the numerical solution towards the screen boundary, with different orders of magnitude, except towards the left-bottom corner, where the solution is trivial.

Figure 13 shows the asymptotic behavior of the numerical solutions at $T = 1$ with respect to the distance r from the left side of the screen, along the green line (on the left) and along the red line (in the center) highlighted on the L-shaped screen and from the re-entrant corner along the red, green and magenta lines (on the right). Here, $\beta = 3$, $L = 16$, have been used. The behavior of the green curve on the left plot is $O(r^{-1/2})$. The red curve in the central plot has a steeper slope $O(r^{-3/4})$, while the three curves on the right plot behave approximately as $O(r^{-1/4})$.

In Table 6 we report the values of the squared energy $\mathcal{E}_L$ of the numerical solution. Figure 14 presents the squared energy errors with respect to the common benchmark $\mathcal{E}_\infty = 0.27029$, which was obtained by extrapolation from the energy values for $\beta = 3$. Again, the convergence rate $\simeq \beta$ is in very good agreement with the theoretical prediction from Section 5.2. Note that the optimal convergence rate is obtained for $\beta = 3$.

Let us note that to reach an accuracy level of $O(10^{-2})$ we need 393.216 space-time DoFs using a uniform mesh, that is, $\beta = 1$, while we need 6.144 space-time DoFs using a graded mesh with $\beta = 2$ and only 768 space-time DoFs using a graded mesh with $\beta = 3$.

10970207, 2025, 20, Downloaded from https://onlinelibrary.wiley.com/doi/10.1002/nme.70163 by University Degli Studi Di Messina, Wiley Online Library on [16/11/2026]. See the Terms and Conditions (https://onlinelibrary.wiley.com/terms-and-conditions) on Wiley Online Library for rules of use; OA articles are governed by the applicable Creative Commons License

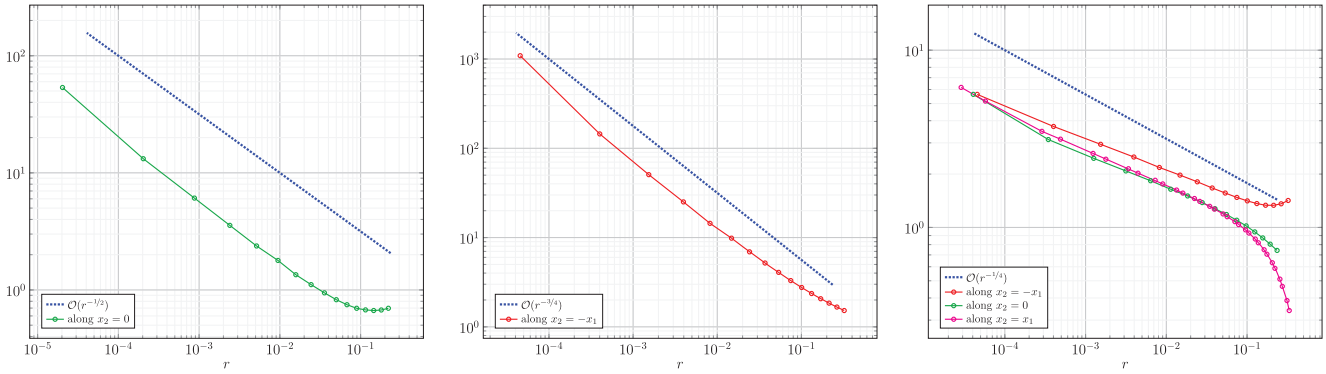

FIGURE 13 | Example 3. Asymptotic behavior of the numerical solution ($L = 16$) for $\beta = 3$, along the red, green and magenta lines highlighted in the L-shaped screen. The plot on the right is with respect to the distance r from the left side of the screen, the plot in the center is with respect to the distance r from the top-left corner, while the plot on the right is with respect to the distance r from the re-entrant corner.

TABLE 6 | Example 3. Squared energy values of the numerical solution at $T = 1$ for $\beta = 1, 2, 3$ and different values of L.

L	2	4	6	8	12	16
$\mathcal{E}_L$ ($\beta = 1$)	$2.5292e-01$	$2.6092e-01$	$2.6380e-01$	$2.6531e-01$	$2.6688e-01$	$2.6768e-01$
$\mathcal{E}_L$ ($\beta = 2$)	$2.6034e-01$	$2.6767e-01$	$2.6907e-01$	$2.6957e-01$	$2.6995e-01$	$2.7008e-01$
$\mathcal{E}_L$ ($\beta = 3$)	$2.6504e-01$	$2.6961e-01$	$2.7015e-01$	$2.7024e-01$	$2.7027e-01$	$2.7028e-01$

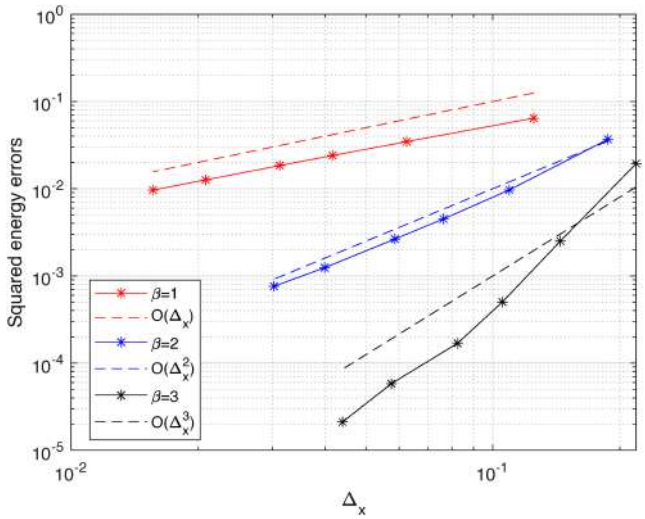

FIGURE 14 | Example 3. Squared errors in energy norm for [$\beta = 1, 2, 3$].

Example 4 (Cone). In this example, we consider the cone $\Gamma := \{(x_1, x_2, x_3) : \sqrt{x_1^2 + x_2^2} \le R \wedge x_3 = (R - \sqrt{x_1^2 + x_2^2})\tan(\omega)\} \cup \{(x_1, x_2, 0) : \sqrt{x_1^2 + x_2^2} \le R\}$, where $\omega = \pi/9$ is the angle between the lateral surface and the disk of radius $R = 0.5$ centered in the origin of the x_1x_2-plane, which represents the cone base. The given datum is $\mathbf{g}(\mathbf{x}; t) = \left(0, 0, \sin^5 t(x_1^2 + x_2^2)/R\right)^\top$. The final time is set $T = 1$, while the material parameters $\varrho = 1$, $\mu = 0.25$ and $\lambda = 0.5$ are taken, in such a way that $c_P = 1$, $c_S = 0.5$, as before.

We introduce on the base of the cone a graded mesh as discussed in Example 2, suitably connected to the mesh constructed on the lateral surface of the 3D domain taken into account, graded towards both the apex and the base of the cone. Along the red line on the lateral surface in Figure 15 on the right, the nodes of the mesh have the following coordinates:

10970207, 2025, 20, Downloaded from https://onlinelibrary.wiley.com/doi/10.1002/nme.70163 by University Degli Studi Di Messina, Wiley Online Library on [16/11/2026]. See the Terms and Conditions (https://onlinelibrary.wiley.com/terms-and-conditions) on Wiley Online Library for rules of use; OA articles are governed by the applicable Creative Commons License

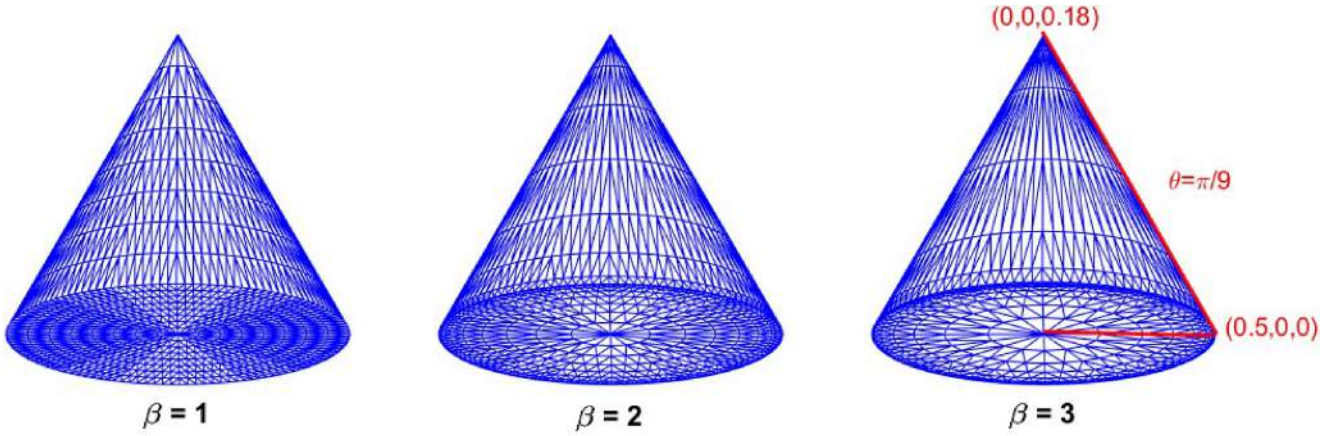

FIGURE 15 | Example 4. Meshes of Γ corresponding to $L = 8$, for $\beta = 1$ (left plot), $\beta = 2$ (center plot) and $\beta = 3$ (right plot).

TABLE 7 | Example 4. Discretization parameters of the cone surface β-meshes with $\beta = 1, 2, 3$, for different values of L.

L	Δ_t	N_{Δ_t}	$\mathscr{E}_{\max}$ $(\beta = 1)$	$\mathscr{E}_{\max}$ $(\beta = 2)$	$\mathscr{E}_{\max}$ $(\beta = 3)$	M_{Δ_x}
4	$1.2500e-01$	8	$1.3302e-01$	$2.1875e-01$	$2.8906e-01$	256
6	$8.3333e-02$	12	$8.8681e-02$	$1.5278e-01$	$2.1065e-01$	864
8	$6.2500e-02$	16	$6.6511e-02$	$1.1719e-01$	$1.6504e-01$	2048
12	$4.1667e-02$	24	$4.4341e-02$	$8.1291e-02$	$1.1487e-01$	6912

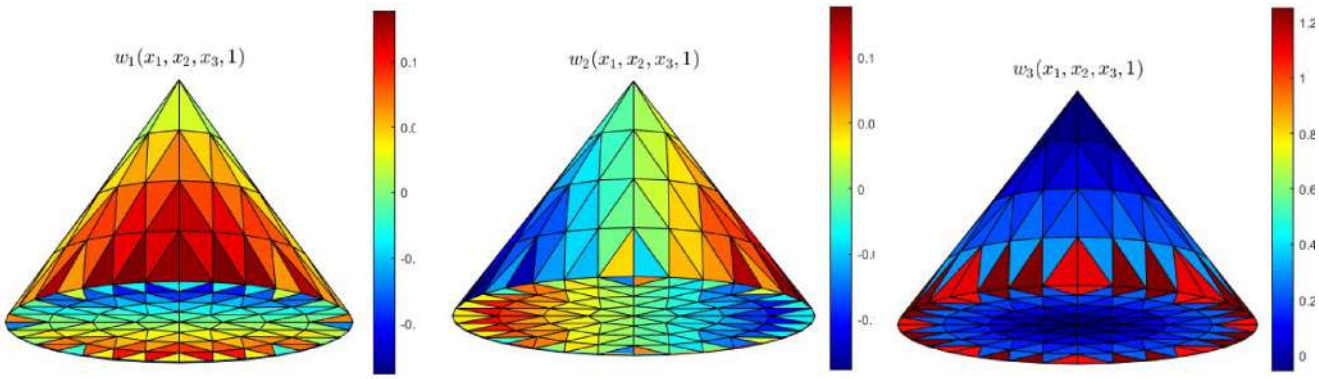

FIGURE 16 | Example 4. For the β-graded mesh with $\beta = 1$ and $L = 4$, from left to right, the components in x_1, x_2, x_3 directions of the numerical solution $\mathbf{w}_{\Delta_x,\Delta_t}$ at the final time $T = 1$ on Γ.

$$\mathbf{x}_1 = \mathbf{0}$$
$$\mathbf{x}_2 = \left[R - \frac{R}{2}\left(\frac{[0:1:(L/2-1)]}{L/2}\right)^{\beta}, \frac{R}{2}, \frac{R}{2}\left(\frac{[(L/2-1):-1:1]}{L/2}\right)^{\beta}, 0\right]$$
$$\mathbf{x}_3 = \mathbf{x}_2 \tan(\omega).$$

Some of the employed discretization parameters for $\beta = 1, 2, 3$ are shown in Table 7.

In Figure 15 the meshes corresponding to $L = 8$ are represented for $\beta = 1$ (left plot), $\beta = 2$ (center plot) and $\beta = 3$ (right plot).

Figure 16 shows the three components of the numerical solution $\mathbf{w}_{\Delta_x,\Delta_t}$ on Γ, at the final time, using $\beta = 1$ and $L = 4$. We observe the singular behavior of the numerical solution towards the circular boundary of the cone base.

10970207, 2025, 20, Downloaded from https://onlinelibrary.wiley.com/doi/10.1002/nme.70163 by University Degli Studi Di Messina, Wiley Online Library on [16/11/2026]. See the Terms and Conditions (https://onlinelibrary.wiley.com/terms-and-conditions) on Wiley Online Library for rules of use; OA articles are governed by the applicable Creative Commons License

Figure 17 shows the numerical solutions at $T = 1$ with respect to the distance r from the circular boundary of the cone base, using $\beta = 1, 2, 3$, $L = 12$. The singular behavior of the solution is of the form $O(r^{\alpha-1})$ with $\alpha = 0.5117$, due to the wedge type singularity at the base of the cone. The singularity at the cone tip is milder, in agreement with the theoretical analysis from Section 3.

In Table 8 we report the values of the squared energy $\mathcal{E}_L$ of the numerical solution. Figure 18 presents the squared energy errors with respect to the common benchmark $\mathcal{E}_\infty = 0.078431$, which was obtained by extrapolation from the energy values for $\beta = 3$. Again, the convergence rate $\simeq \beta$ is in very good agreement with the theoretical prediction from Section 5.2. Note that the optimal convergence rate is obtained for $\beta = 3$, in agreement with (5.4).

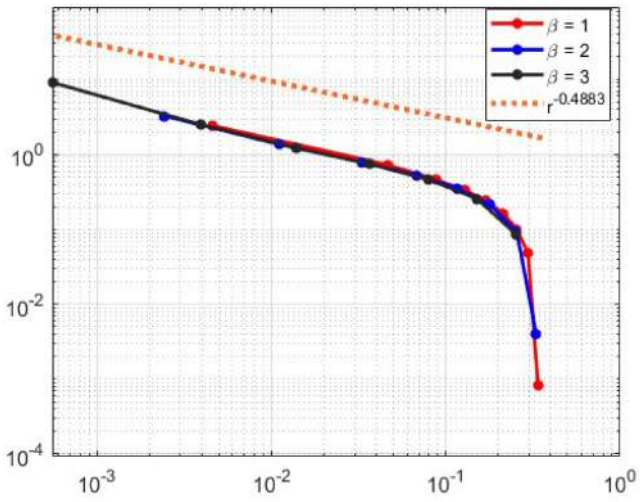

FIGURE 17 | Example 4. Asymptotic behavior of the numerical solution ($L = 12$) for $\beta = 1, 2, 3$. The plot is with respect to the distance r from the circular boundary of the cone base.

TABLE 8 | Example 4. Squared energy values of the numerical solution at $T = 1$ for $\beta = 1, 2, 3$ and different values of L.

L	4	6	8	12
$\mathcal{E}_L$ $(\beta = 1)$	$7.0039e-02$	$7.4195e-02$	$7.5435e-02$	$7.6664e-02$
$\mathcal{E}_L$ $(\beta = 2)$	$7.5018e-02$	$7.7361e-02$	$7.7864e-02$	$7.8177e-02$
$\mathcal{E}_L$ $(\beta = 3)$	$7.6682e-02$	$7.8143e-02$	$7.8332-02$	$7.8395e-02$

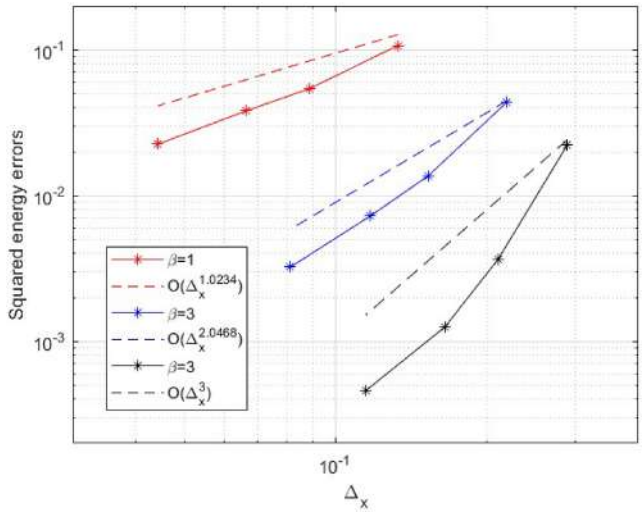

FIGURE 18 | Example 4. Squared errors in energy norm for $\beta = 1, 2, 3$.

10970207, 2025, 20, Downloaded from https://onlinelibrary.wiley.com/doi/10.1002/nme.70163 by University Degli Studi Di Messina, Wiley Online Library on [16/11/2026]. See the Terms and Conditions (https://onlinelibrary.wiley.com/terms-and-conditions) on Wiley Online Library for rules of use; OA articles are governed by the applicable Creative Commons License

To conclude, we observe that to reach an accuracy level of $O(10^{-2})$ we need 165.888 space-time DoFs using a uniform mesh, that is, $\beta = 1$, while we need 10.368 space-time DoFs using a graded mesh with $\beta = 2$ and only 2.048 space-time DoFs using a graded mesh with $\beta = 3$.

Example 5 (Top-down ice-cream geometry). In this example, we consider $\Gamma := \{(x_1, x_2, x_3) : \sqrt{x_1^2 + x_2^2} \leq R \ \wedge \ x_3 = (R - \sqrt{x_1^2 + x_2^2})\tan(\omega)\} \ \cup \ \{(x_1, x_2, x_3) : \sqrt{x_1^2 + x_2^2} \leq R \ \wedge \ x_3 = -\sqrt{R^2 - x_1^2 - x_2^2}\}$, constituted by a cone whose angle with x_1x_2-plane is $\omega = 9\pi/20$ with a hemispherical base of radius $R = 0.5$. The given datum is $\mathbf{g}(\mathbf{x}; t) = \left(0, 0, \sin^5 t(1 - (x_1^2 + x_2^2)/R)\right)^\top$. The final time is set $T = 1$, while the material parameters $\varrho = 1$, $\mu = 0.25$ and $\lambda = 0.5$ are taken, in such a way that $c_P = 1$, $c_S = 0.5$, as before.

We introduce on the hemisphercal surface graded meshes inherited by the graded meshes on the disk as considered in Example 2, suitably connected to the mesh constructed on the lateral surface of the cone part taken into account, graded, similarly to what happens in Example 4, towards both the apex and the hemisphere. Some of the employed discretization parameters for $\beta = 1, 2, 3$ are shown in Table 9:

In Figure 19 the meshes corresponding to $L = 6$ are represented for $\beta = 1$ (left plot), $\beta = 2$ (center plot) and $\beta = 3$ (right plot).

Figure 20 shows the three components of the numerical solution $\mathbf{w}_{\Delta_x, \Delta_t}$ on Γ, at the final time. These results are obtained by considering a β-graded mesh with $\beta = 3$ for $L = 6$. We observe the singular behavior of the numerical solution towards the apex of the top-down ice-cream geometry.

Moreover, the singular behavior of the numerical solutions for $\beta = 1, 2, 3$, $L = 12$, at $T = 1$, is shown in Figure 21. The plot is with respect to the distance r from the apex of the domain. This behavior turns out to be $O(r^{\tilde{\alpha}-1})$ with $\tilde{\alpha} = 0.23189$ due to the prevailing cone (apex) singularity, and follows the theoretical prediction from Section 3.

In Table 10 we report the values of the squared energy $\mathcal{E}_L$ of the numerical solution. Figure 22 presents the squared energy errors with respect to the common benchmark $\mathcal{E}_\infty = 1.5153$, which was obtained by extrapolation from the energy values

TABLE 9 | Example 5. Discretization parameters of the domain surface β-meshes with $\beta = 1, 2, 3$, for different values of L.

L	Δ_t	N_{Δ_t}	$\ell_{\max}$ $(\beta = 1)$	$\ell_{\max}$ $(\beta = 2)$	$\ell_{\max}$ $(\beta = 3)$	M_{Δ_x}
4	$1.2500e-01$	8	$7.9906e-01$	$1.1986e+00$	$1.3983e+00$	256
6	$8.3333e-02$	12	$5.3270e-01$	$8.8784e-01$	$1.1246e+00$	864
8	$6.2500e-02$	16	$3.9953e-01$	$6.9917e-01$	$9.2391e-01$	2048
12	$4.1667e-02$	24	$2.6635e-01$	$4.8831e-01$	$6.7328e-01$	6912

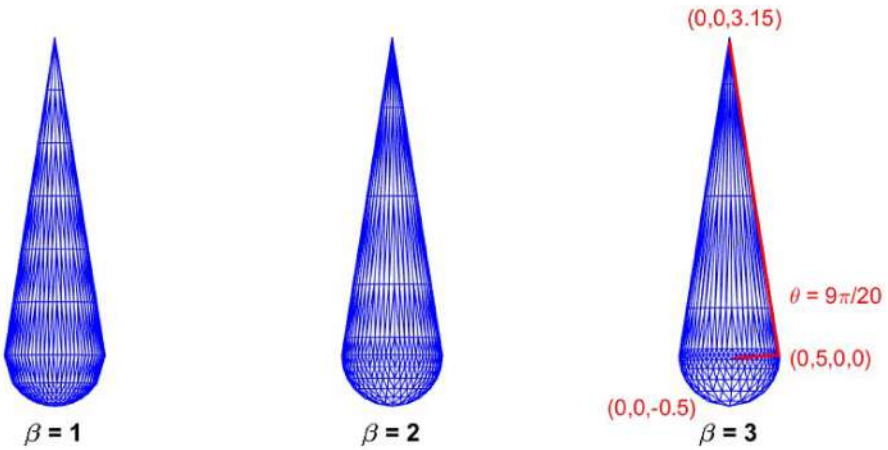

FIGURE 19 | Example 5. Meshes of Γ corresponding to $L = 6$, for $\beta = 1$ (left plot), $\beta = 2$ (center plot) and $\beta = 3$ (right plot).

10970207, 2025, 20, Downloaded from https://onlinelibrary.wiley.com/doi/10.1002/nme.70163 by University Degli Studi Di Messina, Wiley Online Library on [16/11/2026]. See the Terms and Conditions (https://onlinelibrary.wiley.com/terms-and-conditions) on Wiley Online Library for rules of use; OA articles are governed by the applicable Creative Commons License

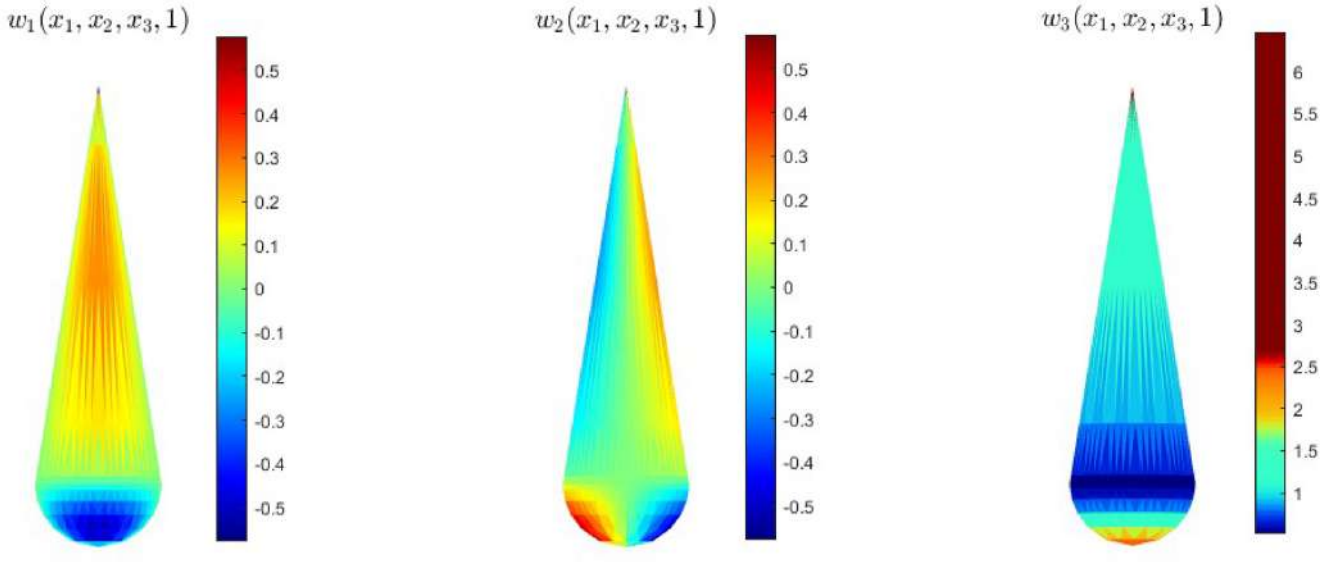

FIGURE 20 | Example 5. For the β-graded mesh with $\beta = 3$ and $L = 6$, from left to right, the components in x_1, x_2, x_3 directions of the numerical solution $\mathbf{w}_{\Delta_x,\Delta_t}$ at the final time $T = 1$ on Γ.

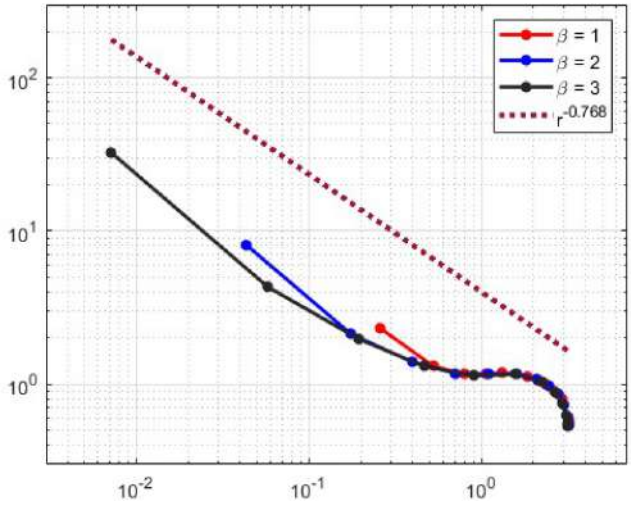

FIGURE 21 | Example 5. Asymptotic behavior of the numerical solution ($L = 12$) for $\beta = 1, 2, 3$. The plot is with respect to the distance r from the apex of the domain.

TABLE 10 | Example 5. Squared energy values of the numerical solution at $T = 1$ for $\beta = 1, 2, 3$ and different values of L.

L	4	6	8	12
$\mathcal{E}_L$ ($\beta = 1$)	$1.4847e+00$	$1.5023e+00$	$1.5079e+00$	$1.5117e+00$
$\mathcal{E}_L$ ($\beta = 2$)	$1.4908e+00$	$1.5060e+00$	$1.5106e+00$	$1.5135e+00$
$\mathcal{E}_L$ ($\beta = 3$)	$1.4901e+00$	$1.5067e+00$	$1.5115e+00$	$1.5142e+00$

for $\beta = 3$. Again, the convergence rate $\simeq \beta$ is in very good agreement with the theoretical prediction from Section 5.2. Note that the optimal convergence rate is obtained for $\beta = 3$, as can be deduced from (5.4) with $\alpha = \tilde{\alpha} + 1/2 = 0.73189$.

Finally, we note that to reach an accuracy level of about 2×10^{-3} we need 165.888 space-time DoFs using a uniform mesh, that is, $\beta = 1$, while we need 32.768 space-time DoFs using graded meshes with $\beta = 2, 3$. Even if the gain is not so high as in the previous examples, the ratio between the two DoFs is about $1/5$.

10970207, 2025, 20, Downloaded from https://onlinelibrary.wiley.com/doi/10.1002/nme.70163 by University Degli Studi Di Messina, Wiley Online Library on [16/11/2026]. See the Terms and Conditions (https://onlinelibrary.wiley.com/terms-and-conditions) on Wiley Online Library for rules of use; OA articles are governed by the applicable Creative Commons License

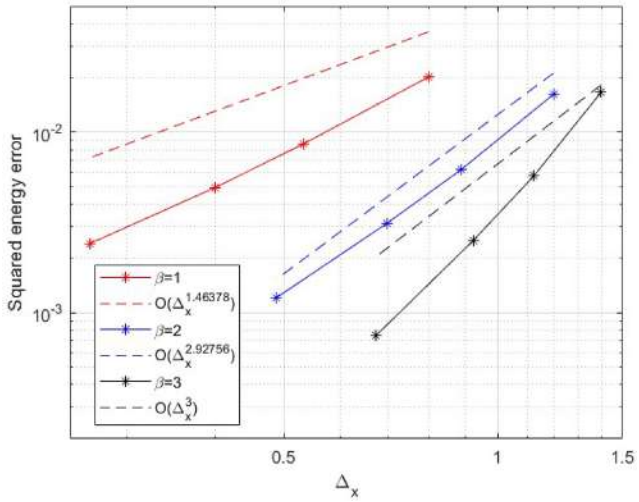

FIGURE 22 | Example 5. Squared errors in energy norm for $\beta = 1, 2, 3$.

7 | Conclusions

This article reduced boundary value problems for 3D time-domain elastodynamics, with a Dirichlet-type boundary and null initial conditions, to time dependent weakly singular boundary integral equations. Guided by the singular behavior of the solution near cone points, corners and edges proposed in [9], we numerically studied a space-time energetic boundary element method on graded meshes. Extensive numerical results confirmed the performance of the approach and the theoretically predicted, quasi-optimal convergence rates. The singular behavior of the solutions is reliably computed, allowing a study of the singular exponents for the time dependent elastic problem. The experiments demonstrate the efficiency and large computational savings using graded meshes. They further confirm the possible use of large time steps, in spite of the resulting locally large CFL ratios, as well as relevant aspects of the numerical quadrature.

Acknowledgments

Parts of this research were supported by the Research in Residence program of the Centre International de Rencontres Mathématiques, Luminy, in 2023. This work was performed as part of the GNCS-INdAM 2025 research program *High-order BEM based numerical techniques for wave propagation problems* (CUP E53C24001950001). Luca Desiderio acknowledges the financial support provided by the European Union *Next GenerationEU*, in the framework of the project *Strategie HPC e modelli fisico-numerici per la previsione di eventi meteorologici estremi* (HPC-XTREME) from the National Recovery and Resilience Plan, Mission 4 'Istruzione e ricerca' Component 2 'Dalla ricerca alla impresa'—Investment 1.4—NATIONAL CENTER FOR HPC, BIG DATA AND QUANTUM COMPUTING (Project Code CN00000013 - CUP B83C22002830001). The views and opinions expressed are solely those of the authors and do not necessarily reflect those of the European Union, nor can the European Union be held responsible for them. Open Access funding provided by Universitat Innsbruck/KEMÖ.

Data Availability Statement

Data sharing not applicable to this article as no datasets were generated or analyzed during the current study.

References

1. M. Dauge, "Elliptic Boundary Value Problems in Corner Domains," in *Lecture Notes in Mathematics*, vol. 1341 (Springer-Verlag, 1988).

2. P. Grisvard, "Singularités en Elasticité," *Archive for Rational Mechanics and Analysis* 107 (1989): 157–180.

3. V. A. Kondratiev, "Boundary Value Problems for Elliptic Equations in Domains With Conical or Angular Points," *Transactions of the Moscow Mathematical Society* 16 (1967): 227–313.

4. C. Schwab, p- *and* hp-*Finite Element Methods: Theory and Applications in Solid and Fluid Mechanics* (Oxford University Press, 1998).

5. J. Gwinner and E. P. Stephan, *Advanced Boundary Element Methods–Treatment of Boundary Value, Transmission and Contact Problems*. Springer Series in Computational Mathematics, vol. 52 (Springer International Publishing, 2018).

10970207, 2025, 20, Downloaded from https://onlinelibrary.wiley.com/doi/10.1002/nme.70163 by University Degli Studi Di Messina, Wiley Online Library on [16/11/2026]. See the Terms and Conditions (https://onlinelibrary.wiley.com/terms-and-conditions) on Wiley Online Library for rules of use; OA articles are governed by the applicable Creative Commons License

6. D. Korikov, B. Plamenevskiĭ, and O. Sarafanov, "Asymptotic Theory of Dynamic Boundary Value Problems in Irregular Domains," in *Operator Theory: Advances and Applications*, vol. 284 (Springer Nature, 2021).

7. S. I. Matyukevich and B. A. Plamenevskiĭ, "Elastodynamics in Domains With Edges," *St. Petersburg Mathematical Journal* 18 (2007): 459–510.

8. F. Müller and C. Schwab, "Finite Elements With Mesh Refinement for Elastic Wave Propagation in Polygons," *Mathematical Methods in the Applied Sciences* 39 (2016): 5027–5042.

9. A. Aimi, G. Di Credico, H. Gimperlein, and E. P. Stephan, "Higher-Order Time Domain Boundary Elements for Elastodynamics–Graded Meshes and Hp-Versions," *Numerische Mathematik* 154 (2023): 35–101.

10. P. Bansal, A. Moiola, I. Perugia, and C. Schwab, "Space-Time Discontinuous Galerkin Approximation of Acoustic Waves With Point Singularities," *IMA Journal of Numerical Analysis* 41 (2021): 2056–2109.

11. V. T. Luong and N. T. Tung, "The Dirichlet-Cauchy Problem for Nonlinear Hyperbolic Equations in a Domain With Edges," *Nonlinear Analysis* 125 (2015): 457–467.

12. F. Müller, D. Schötzau, and C. Schwab, "Discontinuous Galerkin Methods for Acoustic Wave Propagation in Polygons," *Journal of Scientific Computing* 77 (2018): 1–27.

13. I. Perugia, C. Schwab, and M. Zank, "Exponential Convergence of Hp-Time-Stepping in Space-Time Discretizations of Parabolic PDEs," *ESAIM. Mathematical Modelling and Numerical Analysis* 57 (2023): 29–67.

14. H. Gimperlein, F. Meyer, C. Özdemir, D. Stark, and E. P. Stephan, "Boundary Elements With Mesh Refinements for the Wave Equation," *Numerische Mathematik* 139 (2018): 867–912.

15. L. Banjai and F.-J. Sayas, *Integral Equation Methods for Evolutionary PDE*. Springer Series in Computational Mathematics (Springer, 2021).

16. M. Costabel and F.-J. Sayas, "Time-Dependent Problems With the Boundary Integral Equation Method," in *Encyclopedia of Computational Mechanics, Second Edition*, ed. E. Stein, R. de Borst, and T. J. R. Hughes (John Wiley & Sons, 2017).

17. H. Gimperlein, M. Maischak, and E. P. Stephan, "Adaptive Time Domain Boundary Element Methods and Engineering Applications," *Journal of Integral Equations and Applications* 29 (2017): 75–105.

18. T. Ha Duong, "On Retarded Potential Boundary Integral Equations and Their Discretizations," in *Topics in Computational Wave Propagation*. Lecture Notes in Computational Science and Engineering, vol. 31 (Springer, 2003), 301–336.

19. A. Aimi, M. Diligenti, C. Guardasoni, I. Mazzieri, and S. Panizzi, "An Energy Approach to Space-Time Galerkin BEM for Wave Propagation Problems," *International Journal for Numerical Methods in Engineering* 80, no. 9 (2009): 1196–1240.

20. H. Antes, "A Boundary Element Procedure for Transient Wave Propagations in Two-Dimensional Isotropic Elastic Media," *Finite Elements in Analysis and Design* 1 (1985): 313–322.

21. E. Bécache, "A Variational Boundary Integral Equation Method for an Elastodynamic Antiplane Crack," *International Journal for Numerical Methods in Engineering* 36 (1993): 969–984.

22. E. Bécache and T. Ha Duong, "A Space-Time Variational Formulation for the Boundary Integral Equation in a 2d Elastic Crack Problem," *ESAIM. Mathematical Modelling and Numerical Analysis* 28 (1994): 141–176.

23. A. Aimi, S. Dallospedale, L. Desiderio, and C. Guardasoni, "A Space-Time Energetic BIE Method for 3D Elastodynamics. The Dirichlet Case," *Computational Mechanics* 72 (2023): 885–905.

24. S. Chaillat and M. Bonnet, "Recent Advances on the Fast Multipole Accelerated Boundary Element Method for 3D Time-Harmonic Elastodynamics," *Wave Motion* 50 (2013): 1090–1104.

25. L. Desiderio, "An $\mathcal{H}$-Matrix Based Direct Solver for the Boundary Element Method in 3D Elastodynamics," *AIP Conference Proceedings* 1978 (2018): 120005.

26. S. Falletta, G. Monegato, and L. Scuderi, "Two Boundary Integral Equation Methods for Linear Elastodynamics," *IMA Journal of Numerical Analysis* 34, no. 1 (2014): 390–434.

27. M. Schanz, W. Ye, and J. Xiao, "Comparison of the Convolution Quadrature Method and Enhanced Inverse FFT With Application in Elastodynamic Boundary Element Method," *Computational Mechanics* 57 (2016): 523–536.

28. T. Apel, V. Mehrmann, and D. Watkins, "Structured Eigenvalue Methods for the Computation of Corner Singularities in 3D Anisotropic Elastic Structures," *Computer Methods in Applied Mechanics and Engineering* 191 (2002): 4459–4473.

29. T. Apel, A.-M. Sändig, and S. I. Solov'ev, "Computation of 3D Vertex Singularities for Linear Elasticity: Error Estimates for a Finite Element Method on Graded Meshes," *ESAIM. Mathematical Modelling and Numerical Analysis* 36 (2002): 1043–1070.

30. Z. P. Bazant and L. M. Keer, "Singularities of Elastic Stresses and of Harmonic Functions at Conical Notches or Inclusions," *International Journal of Solids and Structures* 10 (1974): 957–964.

10970207, 2025, 20, Downloaded from https://onlinelibrary.wiley.com/doi/10.1002/nme.70163 by University Degli Studi Di Messina, Wiley Online Library on [16/11/2026]. See the Terms and Conditions (https://onlinelibrary.wiley.com/terms-and-conditions) on Wiley Online Library for rules of use; OA articles are governed by the applicable Creative Commons License

31. A. E. Beagles and A.-M. Sändig, "Singularities of Rotationally Symmetric Solutions of Boundary Value Problems for the Lamé Equations," *Zeitschrift für Angewandte Mathematik und Mechanik* 71 (1991): 423–431.

32. M. Costabel, M. Dauge, and Z. Yosibash, "A Quasidual Function Method for Extracting Edge Stress Intensity Functions," *SIAM Journal on Mathematical Analysis* 35 (2004): 1177–1202.

33. N. Omer and Z. Yosibash, "Singular Asymptotic Expansion of the Elastic Solution Along an Edge Around Which Material Properties Depend on the Angular Coordinate," *Mathematics and Mechanics of Solids* 22 (2017): 2288–2308.

34. T. von Petersdorff and E. P. Stephan, "Regularity of Mixed Boundary Value Problems in $\mathbb{R}^{<i>3</i>}$ < i > and Boundary Element Methods on Graded Meshes," *Mathematical Methods in the Applied Sciences* 12 (1990): 229–249.

35. I. Babuska, R. B. Kellogg, and J. Pitkäranta, "Direct and Inverse Error Estimates for Finite Elements With Mesh Refinements," *Numerische Mathematik* 33 (1979): 447–471.

36. C. Bacuta, V. Nistor, and L. T. Zikatanov, "Improving the Rate of Convergence of 'High Order Finite Elements' on Polygons and Domains With Cusps," *Numerische Mathematik* 36 (2005): 165–184.

37. T. Apel, S. Nicaise, and J. Schöberl, "Finite Element Methods With Anisotropic Meshes Near Edges," in *Finite Element Methods*. GAKUTO International Series. Mathematical Sciences and Applications, vol. 15 (Gakkotosho, 2000).

38. H. Li, *Graded Finite Element Methods for Elliptic Problems in Nonsmooth Domains* (Springer Nature, 2022).

39. L. Monasse and C. Mariotti, "An Energy-Preserving Discrete Element Method for Elastodynamics," *ESAIM. Mathematical Modelling and Numerical Analysis* 46 (2012): 1527–1553.

40. P. Grisvard, "Edge Behavior of the Solution of an Elliptic Problem," *Mathematische Nachrichten* 132 (1987): 281–299.

41. H. Gimperlein, C. Özdemir, D. Stark, and E. P. Stephan, "Hp-Version Time Domain Boundary Elements for the Wave Equation on Quasi-Uniform Meshes," *Computer Methods in Applied Mechanics and Engineering* 356 (2019): 145–174.

42. H. Gimperlein, C. Özdemir, D. Stark, and E. P. Stephan, "A Residual a Posteriori Error Estimate for the Time–Domain Boundary Element Method," *Numerische Mathematik* 146 (2020): 239–280, https://doi.org/10.1007/s00211-020-01142-y.

43. L. Xu and T. Kundu, "Stress Singularities at Crack Corners," *Journal of Elasticity* 39 (1995): 1–16.

44. D. Colton, *Partial Differential Equations: An Introduction* (Random House, 1988).

45. R. B. Guenther and J. W. Lee, *Partial Differential Equations of Mathematical Physics and Integral Equations* (Prentice-Hall, 1988).

46. I. Terrasse, *RéSolution Mathématique et Numérique Des équations de Maxwell Instationnaires Par Une Méthode de Potentiels Retardés*, Ph.D. thesis (École Polytechnique, 1993).

47. V. J. Ervin and E. P. Stephan, "A Boundary-Element Method With Mesh Refinement for a Weakly Singular Integral Equation," *Communications in Applied Numerical Methods* 7 (1991): 273–280.

48. F. D. Gaspoz and P. Morin, "Convergence Rates for Adaptive Finite Elements," *IMA Journal of Numerical Analysis* 29 (2009): 917–936.

49. L. Coppolino and L. Desiderio, "Space-Time Energetic Galerkin BEM for the Numerical Solution of 3D Elastodynamic Problems: Overcoming Challenges of the Strongly Singular Integral Operator," in *Computational Mechanics* (Springer, 2025), https://doi.org/10.1007/s00466-025-02668-4.

50. A. Aimi, M. Diligenti, A. Frangi, and C. Guardasoni, "Energetic BEM-FEM Coupling for Wave Propagation in 3D Multidomains," *International Journal for Numerical Methods in Engineering* 97 (2014): 377–394.

51. H. Xiao and Z. Gimbutas, "A Numerical Algorithm for the Construction of Efficient Quadrature Rules in Two and Higher Dimensions," *Computers & Mathematics With Applications* 59 (2010): 663–676.

52. T. von Petersdorff, *Randwertprobleme der Elastizitätstheorie für Polyeder-Singularitäten und Approximation mit Randelementmethoden*, Ph.D. thesis (Technische Universität Darmstadt, 1989).

Appendix A

Let $L^2(\widetilde{\Gamma})$ be the space of measurable functions whose square is Lebesgue integrable on $\widetilde{\Gamma}$. The inner product and the norm of this space are defined respectively by:

$$\langle u, v\rangle_{L^2(\widetilde{\Gamma})} := \int_{\widetilde{\Gamma}} u(\mathbf{x})v(\mathbf{x})\mathrm{d}\Gamma_{\mathbf{x}} \qquad \text{and} \qquad \|u\|_{L^2(\widetilde{\Gamma})} := \sqrt{\langle u, u\rangle_{L^2(\widetilde{\Gamma})}} \qquad \forall u, v \in L^2(\widetilde{\Gamma}).$$

Now, we recall that at each point $\mathbf{x} \in \widetilde{\Gamma}$ there is an open neighbourhood U and a bijective mapping $\phi : U \to Q$, where $Q \subset \mathbb{R}^3$ is the unit cube centered at the origin. Consequently, $\widetilde{\Gamma}$ can be covered by a finite set $\{U_i\}_{i=1}^k$ of such neighbourhoods, whose corresponding maps form a finite family of diffeomorphisms $\{\phi_i\}_{i=1}^k$. If we denote by $\{\alpha_i\}_{i=1}^k$ a partition of unity subordinate to the covering $\{U_i\}_{i=1}^k$, any function $u : \widetilde{\Gamma} \to \mathbb{R}$ can be written in the form

10970207, 2025, 20, Downloaded from https://onlinelibrary.wiley.com/doi/10.1002/nme.70163 by University Degli Studi Di Messina, Wiley Online Library on [16/11/2026]. See the Terms and Conditions (https://onlinelibrary.wiley.com/terms-and-conditions) on Wiley Online Library for rules of use; OA articles are governed by the applicable Creative Commons License

$$u(\mathbf{x}) = \sum_{i=1}^{k} \alpha_i(\mathbf{x}) u(\mathbf{x}) \qquad \forall \mathbf{x} \in \widetilde{\Gamma}$$

and each summand can be parametrized over $\phi_i(U_i \cap \widetilde{\Gamma}) \subset \mathbb{R}^2$ as $(\alpha_i u) \circ \phi_i^{-1}$. After these preparatory remarks, for each $s \in \mathbb{R}$ we introduce the Sobolev space

$$\mathrm{H}^s(\widetilde{\Gamma}) := \left\{ u : \widetilde{\Gamma} \to \mathbb{R} \mid (\alpha_i u) \circ \phi_i^{-1} \in \mathrm{H}^s(\phi_i(U_i \cap \widetilde{\Gamma})),\ \forall i = 1, \dots, k \right\}$$

that becomes a Hilbert space once it is equipped with the norm

$$\|u\|_{s,\widetilde{\Gamma}} := \sqrt{\sum_{i=1}^{k} \|(\alpha_i u) \circ \phi_i^{-1}\|^2_{\mathrm{H}^s(\phi_i(U_i \cap \widetilde{\Gamma}))}} \ .$$

The value of the above norm clearly depends on the choice of U_i, α_i and ϕ_i, but one can show that the resulting norms will be equivalent and that the space $\mathrm{H}^s(\widetilde{\Gamma})$ is independent of this choice. Furthermore, for every parameter $\omega = \rho + \imath\sigma \in \mathbb{C} \setminus \{0\}$, we introduce ω-dependent norms for $\mathrm{H}^s(\widetilde{\Gamma})$, that is,

$$\|u\|_{s,\omega,\widetilde{\Gamma}} := \sqrt{\sum_{i=1}^{k} \int_{\mathbb{R}^2} \left(|\omega|^2 + |\xi|^2\right)^s \left|\mathcal{F}\{(\alpha_i u) \circ \phi_i^{-1}\}(\xi)\right|^2 \mathrm{d}\xi}$$

where $\mathcal{F}$ stands for the Fourier transform. Note that, by varying ω, each $\|\cdot\|_{s,\omega,\widetilde{\Gamma}}$ is equivalent to $\|\cdot\|_{s,\widetilde{\Gamma}}$.

At this stage, we call $\widetilde{\mathrm{H}}^s(\Gamma)$ the closed subspace of $\mathrm{H}^s(\widetilde{\Gamma})$ collecting all the distributions with support in $\overline{\Gamma}$, and we denote by $\mathrm{H}^s(\Gamma)$ the quotient space $\mathrm{H}^s(\widetilde{\Gamma})/\widetilde{\mathrm{H}}^s(\widetilde{\Gamma} \setminus \overline{\Gamma})$. We use the norm $\|\cdot\|_{s,\omega,\widetilde{\Gamma}}$ in order to define a norm on $\mathrm{H}^s(\widetilde{\Gamma})$, that is,

$$\|u\|_{s,\omega,\Gamma} := \inf_{h \in \widetilde{H}^s(\widetilde{\Gamma} \setminus \overline{\Gamma})} \|u + h\|_{s,\omega,\widetilde{\Gamma}} \qquad \forall u \in \mathrm{H}^s(\widetilde{\Gamma}).$$

and a norm on $\mathrm{H}^s(\Gamma)$, that is,

$$\|u\|_{s,\omega,\Gamma,*} := \|e^+(u)\|_{s,\omega,\widetilde{\Gamma}} \qquad \forall u \in \mathrm{H}^s(\Gamma),$$

e^+ being the operator that extends the distribution f by 0 from Γ to $\widetilde{\Gamma}$. Note that, for a fixed ω, the norm $\|\cdot\|_{s,\omega,\Gamma,*}$ is stronger than $\|\cdot\|_{s,\omega,\Gamma}$, whenever $s \in \frac{1}{2} + \mathbb{Z}$.

For a given $\sigma > 0$ and two parameters $s, p \in \mathbb{R}$, we define the space-time anisotropic Sobolev spaces:

$$\mathrm{H}^p_\sigma\left(\mathbb{R}^+; \mathrm{H}^s(\Gamma)\right) := \left\{ f \in \mathcal{D}'_+(\mathrm{H}^s(\Gamma)) \ : \ e^{-\Im\omega t} f \in \mathcal{S}'_+(\mathrm{H}^s(\Gamma)) \quad \text{and} \quad \|f\|_{s,\omega,\Gamma} < +\infty \right\}$$
$$\mathrm{H}^p_\sigma\left(\mathbb{R}^+; \widetilde{\mathrm{H}}^s(\Gamma)\right) := \left\{ f \in \mathcal{D}'_+(\widetilde{H}^s(\Gamma)) \ : \ e^{-\Im\omega t} f \in \mathcal{S}'_+(\widetilde{H}^s(\Gamma)) \quad \text{and} \quad \|f\|_{s,\omega,\Gamma,*} < +\infty \right\}$$

where $\mathcal{D}'_+(E)$ denotes the space of all the distributions on $\mathbb{R}$ with support in $[0, +\infty)$, taking values in a Hilbert space E, while its subspace $\mathcal{S}'_+(E) \subset \mathcal{D}'_+(E)$ contains all the tempered distributions. In these two spaces the norms are given respectively by:

$$\|f\|_{p,s,\Gamma} := \sqrt{\int_{-\infty+\imath\sigma}^{+\infty+\imath\sigma} |\omega|^{2p} \ \|\mathcal{F}\{f\}(\omega)\|^2_{s,\omega,\Gamma} \ \mathrm{d}\omega}$$
$$\|f\|_{p,s,\Gamma,*} := \sqrt{\int_{-\infty+\imath\sigma}^{+\infty+\imath\sigma} |\omega|^{2p} \ \|\mathcal{F}\{f\}(\omega)\|^2_{s,\omega,\Gamma,*} \ \mathrm{d}\omega}.$$

We remark that, for $p = s = 0$, $\mathrm{H}^p_\sigma\left(\mathbb{R}^+; \mathrm{H}^s(\Gamma)\right)$ and $\mathrm{H}^p_\sigma\left(\mathbb{R}^+; \widetilde{\mathrm{H}}^s(\Gamma)\right)$ correspond to the weighted L^2-space with standard inner product. For 3D vector-valued functions in space variable, we denote by $\mathrm{H}^p_\sigma\left(\mathbb{R}^+; \mathrm{H}^s(\Gamma)\right)^3$ and $\mathrm{H}^p_\sigma\left(\mathbb{R}^+; \widetilde{\mathrm{H}}^s(\Gamma)\right)^3$ the extension of the previously introduced functional spaces.

10970207, 2025, 20, Downloaded from https://onlinelibrary.wiley.com/doi/10.1002/nme.70163 by University Degli Studi Di Messina, Wiley Online Library on [16/11/2026]. See the Terms and Conditions (https://onlinelibrary.wiley.com/terms-and-conditions) on Wiley Online Library for rules of use; OA articles are governed by the applicable Creative Commons License